國立臺灣大學理學院大氣科學研究所

碩士論文

Department of Atmospheric Sciences

College of Science

National Taiwan University

Master Thesis

地面模式擾動對午後對流系集預報的影響

The Impact of LSM perturbation on Afternoon

Thunderstorm Ensemble Forecast

洪語澤

Yu-Tze Hong

指導教授：陳正平 博士

Advisor: Jen-Ping Chen, Ph.D.

中華民國 112 年 7 月

July 2023

中文摘要

　　Noah Multi Parameterization（Noah MP）是一個社群地面模式（Land surface model，LSM），針對重要地表物理過程，分別發展多種不同物理參數法，並介接多個天氣或氣候模式，作為研發及作業之用。本研究使用 Noah MP 設計以地表模式為主的系集擾動方法，並評估其對午後對流系集預報的影響。

　　本研究首先在離線（Offline）實驗架構下，探討 Noah MP 在台灣地區的起轉（spin-up）特徵以及不同地表物理過程對系集離散度的影響。研究結果顯示，Noah MP 約需至少三個月的起轉時間以達到平衡狀態（equilibrium state）；在敏感性實驗中共測試了五種地表物理過程，結果顯示對系集離散度的貢獻程度依序為：表面熱交換係數、冠層輻射幾何形狀、冠層氣孔阻力、蒸發表面阻力和氣孔阻力的土壤水分因子。本研究取前四種物理過程的參數法，介接大氣預報模式，建構以地表模式為主的系集擾動方法。

　　其次，本研究針對五個午後對流個案，共進行兩個系集實驗，以評估 LSM 擾動對午後對流預報的影響。每個實驗包含 24 個系集成員，第一個實驗只對大氣初始條件進行擾動，另一個實驗則進行了額外加入 LSM 擾動。24 小時預報的結果顯示，加入 LSM 擾動後雖然沒有顯著改善模式系集平均的預報能力，但可以有效增加降雨以及近地表大氣變量系集預報的離散度。本研究進一步分析造成系集成員離散度的根因，結果顯示系集離散度的主要源於表面熱交換係數參數法，而這也導致系集成員產生分群的現象。研究亦指出，適當調校地面模式的熱交換係數參數法，是進一步改善系集預報準確度和離散度的關鍵之一。
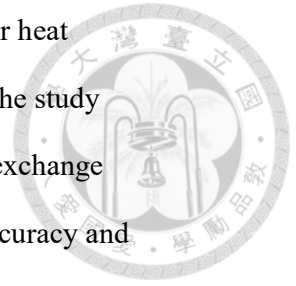
ABSTRACT

Noah Multi Parameterization (Noah MP) is a community land surface model (LSM) that incorporates multiple physics parameterization schemes for important land surface processes. This study utilizes Noah MP to design a LSM-based ensemble perturbation scheme and evaluates its impact on ensemble forecasting of afternoon thunderstorms over Taiwan.

In this study, we first investigate the spin-up characteristics of Noah MP in the offline experimental framework and examine the influence of different land surface physics processes on the ensemble spread. The results indicate that Noah MP requires a spin-up period of at least three months to reach an equilibrium state. The five tested land surface physics processes that contribute to the ensemble spread are ranked in descending order: surface layer heat exchange coefficient, canopy radiation geometry, canopy stomatal resistance, surface resistance to evaporation, and soil moisture factor for stomatal resistance. The parameterization schemes of the first four land surface processes are selected to construct the LSM-based ensemble perturbation scheme.

Next, we conduct two ensemble experiments for five afternoon convection cases to assess the impact of LSM perturbation on afternoon thunderstorms forecasting. Each experiment consists of 24 ensemble members, with the first experiment perturbing only the atmospheric initial conditions and the second experiment incorporating additional LSM perturbations. The 24-hour forecast results show that while the addition of LSM perturbation does not significantly improve the ensemble mean forecast skill, it effectively increases the ensemble spread for rainfall and near-surface atmospheric variables. Further analysis reveals that the main source of

ensemble spread lies in the parameterization scheme of the surface layer heat

exchange coefficient, leading to the clustering of ensemble members. The study

emphasizes the importance of properly calibrating the surface model's exchange

coefficient parameterization scheme as a key factor in enhancing the accuracy and

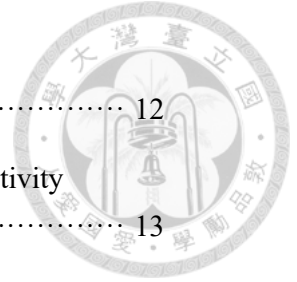spread of ensemble forecasting.

CONTENT

LIST OF TABLES

LIST OF FIGURES

1. Introduction

1.1 Afternoon thunderstorm (AT) in Taiwan

Taiwan, a small subtropical island measuring 400 km long and 150 km wide, features mountains with a nearly north-south orientation extending over 3000 m above sea level (known as the Central Mountain Range or CMR) within 50 km from the coast. In warm seasons, aside from tropical cyclones, most convective systems are afternoon thunderstorms (ATs) (Chen et al., 2014). The Central Weather Bureau (CWB) operates a surface observation network that provides high temporal resolution (up to minutes) and spatial resolution (less than 10 km) data, enabling a detailed near-surface meteorological field resolution and potentially providing an indication of ATs development. However, predicting the precise location, timing, and intensity of ATs with adequate lead time remains challenging.

Land-sea breeze, anabatic flows, and orography effect significantly influence the structure and evolution of ATs in Taiwan (Chen and Li, 1995; Johnson and Bresch, 1991; Lin et al., 2011; Chang et al., 2017). Jou (1994) found that storm outflows can propagate downslope, and the collision between storm outflows and sea breeze can lead to significant intensification near the foothills of the CMR. Additionally, cold pools and outflow boundaries is critical for ATs development, particularly triggering new convective cells (Hirt et al., 2020; Rotunno et al., 1988). Several studies have also demonstrated that the most common moist convection systems occur on the lower slopes of mountains near the coast rather than at higher elevations (Johnson and Bresch, 1991; Chen et al., 2007; Lin et al., 2011). Moreover, Chen et al. (2016) developed a two-step forecast advisory that uses synoptic features and surface meteorological conditions to predict ATs occurrence in northern Taiwan.

To accurately predict ATs initiation, understanding pre-storm environmental characteristics, complex terrain effects, and storm-scale interactions is critical. However, these processes have high nonlinearity and limit the ATs predictability.

1.2 Convective scale predictability

Numerical Weather Prediction (NWP) predictability can be divided into two

parts: practical predictability and intrinsic predictability. Practical predictability refers to how well a model can predict future atmospheric states based on current procedures in NWP. Intrinsic predictability is the limit of predictability with optimal procedures (Zhang et al., 2006; Melhauser and Zhang, 2012). Practical predictability is limited by errors and uncertainties in model numerics, physics, and data assimilation procedures that are identifiable. On the other hand, intrinsic predictability is the limit of predictability that is reached with almost perfect knowledge of the atmospheric initial conditions and NWP model.

The intrinsic predictability limit cannot be overcome due to the chaotic nature of moist convective processes (Melhauser and Zhang, 2012). The practical and intrinsic predictability of the atmosphere depends on the scale of the motion and the specific atmospheric flow patterns (Zhang et al., 2006).

By utilizing convection-permitting numerical models that explicitly resolve moist convection, the prediction of severe convection is expected to improve compared to convective parameterization models (Peters et al., 2019). However, due to the nonlinear nature of rapidly evolving convections, model predictability is limited within a few hours.

Studies have shown that initial conditions' accuracy significantly impacts model predictability (Sokol and Zacharov, 2012; Sun et al., 2012; Tong et al., 2016). Forecast errors also originate from imperfect numerical models. Although knowledge of convective-scale error growth mechanisms is limited, small-scale variability of low-level wind, temperature, and water vapor can all influences precipitation predictability (Weckwerth, 2000). Small-scale perturbations in the planetary boundary layer (PBL) scheme can influence convective initiation, precipitation amount, and location (Hirt and Craig, 2019; Hirt et al., 2021). Similarly, perturbations in microphysics schemes facilitate error growth in areas with larger convective instability (Hermoso et al., 2021; Thompson et al., 2021).

Organized mesoscale convective systems typically involve intense multiscale interaction. Studies have found that small-scale, nonlinear errors quickly grow upscale due to moist convective processes, which limits mesoscale predictability, especially for deterministic model forecasts (Zhang et al., 2002). Therefore, relying solely on the

2

deterministic model usually lead to poor forecasts in some cases. However, ensemble forecasts can overcome some of these predictability problems and provide forecast uncertainty information.
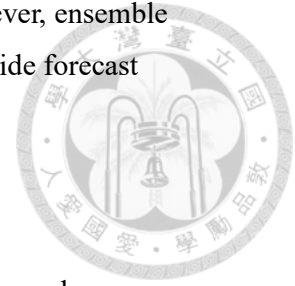
1.3 Uncertainty of land-air interaction

The Land-Air Interaction (LAI) plays a crucial role in the evolution and forecasting of Afternoon Thunderstorms (ATs). Variations in the treatment of land and vegetation processes within LSM have significant impacts on surface sensible and latent heat fluxes, convective mixing, boundary layer growth, and the transport of moisture into the upper troposphere (Anthes, 1984; Duda et al., 2017; Pielke, 2001). Therefore, precisely describing the LAI process in models plays a crucial role in enhancing the simulation of energy exchange between land and atmosphere, as well as subsequent local circulation processes.

Trier et al. (2008) demonstrated that the variation in the initial soil moisture (SM) state has a greater influence on precipitation forecasts than the choice of LSM. Notably, the poor coverage of observations is a significant source of uncertainty in SM analyses. However, even with dense observations, uncertainty in SM persists due to its inherent spatial heterogeneity, even within small areas (Basara, 2001).

While ensuring the accuracy of the initial SM state is crucial for convection forecasts, it is essential to acknowledge the presence of additional uncertainties in the formulation of physical processes related to energy and mass fluxes. Numerous studies have highlighted the sensitivity of precipitation forecasts to the specification of empirical constants used in calculating the thermal roughness length (Chen et al., 1997). Such empirical constants play a vital role in the formulation of the exchange coefficient for estimating the sensible heat flux (Marshall et al., 2003; LeMone et al., 2008; Chen et al., 2010; Trier et al., 2004, 2011).

The computation of latent heat flux from plant transpiration is associated with various uncertainties, as highlighted by numerous studies. One crucial factor is the resistance term, such as the stomatal resistance and generic canopy resistance. This term governs the efficiency with which plants release water through their leaves into the atmosphere and how effectively the water can be transported from the canopy to

the lower atmosphere (Chen and Dudhia, 2001; Jackson et al., 2003; Godfrey and Stensrud, 2010; Kumar et al., 2011). Understanding and accurately modeling the LAI of the canopy process are critical for reliable estimations of latent heat flux and therefore improving the moisture transport processes.
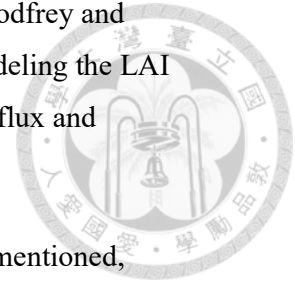
In summary, accurate forecasting of ATs is crucial for Taiwan; as mentioned, improvement of the LAI process in models is vital in enhancing the prediction in local circulation and, of course, is expected to improve the ATs prediction. From another perspective, uncertainties in LAI can potentially affect the evolution of ATs, making it imperative to address the uncertainties associated with LSMs in ATs ensemble forecasts.

However, to improve ensemble forecasts, it is necessary to identify and address the sources of uncertainty in physical processes. LAI plays a significant role among these sources and introduces various uncertainties, such as SM initialization, static data representation, and heat flux calculations.

This study aims to evaluate the uncertainties in the LSM physical processes, configure an LSM-based perturbation scheme, and investigate its impact on the ATs ensemble forecast using the cloud-resolving model. The paper is organized as follows. Section 2 describes the experimental design and methodology, observational data, and validation method. Section 3 introduces the offline experiment result. Section 4 examines the impact of the LSM-based perturbation scheme on the ATs ensemble forecast. Section 5 presents the discussion of the results. A summary is provided in Section 6.

2. Experiment design and data

2.1 Offline Noah MP experiment

The land surface interacts with the atmosphere by exchanging energy, momentum, water, and carbon dioxide, significantly affecting the weather and climate at various spatial and temporal scales (Sellers et al., 1996; Shukla and Mintz, 1982). Over the past three decades, the coupling of the atmospheric and LSMs have become more comprehensive, enabling them to represent increasing interactions and feedbacks between physical, biological, and chemical processes between the land and atmosphere (Pitman, 2003). This study applied the Noah Multi-parameterization LSM (Noah MP) for its comprehensive physical parameterizations.

2.1.1 Noah MP details

The Noah LSM is widely coupled with general circulation models and mesoscale atmospheric models because of its relative simplicity for real-time global and regional weather and hydrology applications (Chen and Dudhia 2001; Ek et al. 2003; Tewari et al. 2016). The Noah LSM has been implemented in the National Centers for Environment Prediction (NCEP) operational Eta Model for global and regional forecasts (Ek et al. 2003). Finally, the Noah LSM is used for research and operational purposes (Hung et al. 2014). An updated version of this model, namely Noah MP, which includes multi-parameterization options, has also been implemented in different mesoscale atmospheric models (Niu et al. 2011). The Noah MP incorporates various parameterization schemes for physical processes within the same dynamic model structure. These physical processes include vegetation phenology, stomatal resistance, runoff, groundwater, soil-moisture factor controlling stomatal resistance, frozen soil and infiltration, surface exchange coefficient, and radiation transfer, among others in Table 2.1. For each process, two to four parameterization schemes are available (Niu et al., 2011; Yang et al., 2011). Therefore, Noah MP is suitable for designing a multi-model LSM ensemble. With a specific combination of physical schemes, it can serve as a surrogate for another LSM, making it a valuable tool for assessing sources of physical process uncertainty in LSMs.

Moreover, multi-model averages have resulted in generally better behavior, as demonstrated in various offline experiments of the Project for Intercomparison of Land Surface Parameterization Schemes (PIPLS) and two phases of the Global Soil Wetness Project (GSWP) (Entin et al., 1999; Guo and Dirmeyer, 2006; Dirmeyer et al., 2006b) and online (coupled to atmospheric models) in GLACE (Dirmeyer et al., 2006a). This indicates that an LSM with multi-physics options offers the potential to mimic multi-model behaviors and is well suited to simulate a range of potential outcomes. Therefore, it is necessary to develop an LSM that accommodates numerous combinations of parameterization schemes to represent the complex processes that occur in nature accurately

2.1.2 Offline experiment setups

An offline LSM experiment refers to a type of simulation in which a LSM is run in isolation from other earth system components, such as the atmosphere and ocean (Koster et al., 2009). In this type of experiment, the LSM is forced with prescribed atmospheric conditions and then allowed to simulate the exchange of energy, water, and carbon between the land surface and the atmosphere. They then run the LSM using input data that represents observed or simulated atmospheric conditions (Fig. 2.1). The purpose of offline LSM experiments is helpful to estimate the accuracy of LSM model and to better understand the physical processes that control the behavior of land surfaces and their interactions with the atmosphere.

As shown in the schematic diagram in Fig. (2.2), we used hourly atmospheric forcing data of 1-km resolution (Fig. 2.3), consisting of temperature, water vapor, wind speed, surface pressure, radiation, and precipitation. Specifically, temperature, water vapor, wind speed, longwave radiation, and surface pressure data were sourced from the 12-23 hour forecast of the 1-km operational CWB-WRF output.

Short wave radiation data was sourced from three channels (B03, B13, and B15) of the Himawari-8 geostationary satellite measurements. The product has a spatial resolution of 0.01° and a temporal resolution of 10 minutes. It took into account astronomical factors between the Sun and Earth, as well as atmospheric gas absorption, cloud extinction, and aerosol optical thickness in the Earth's atmosphere

6

(Cheng et al., 2021).

Precipitation data were obtained from radar quantitative precipitation estimation (QPE). The QPE product was adopted from the Quantitative Precipitation Estimation and Segregation Using Multiple Sensors (QPESUMS) system (Chang et al. 2021). This QPESUMS QPE is derived by an empirical Z–R relation explicitly designed for the Taiwan area with additional rain gauge correction to remove errors and biases.

The land surface characteristic data, for example, soil texture, land cover, vegetation fraction, and terrain height, significantly influenced LAI. This study collected data from various sources and applied it to the WRF Preprocess System (WPS) static dataset.

- Soil texture: the soil texture data were adopted from Lin and Cheng (2016), which were collected from the Council of Agriculture, Executive Yuan, with vector-format (polygon) data for 1/50 000–1/25 000 soil maps (available online at http://taiwansoil.tari.gov.tw/Web.Net2008/index_1/main1-1.aspx)
- Terrain height: the terrain height data were adopted from the updated 20-m resolution 2020 Taiwan Digital Terrain Model (DTM) dataset provided by the Ministry of the Interior and the Central Geological Survey of the Ministry of Economic Affairs.
- Land cover: land cover data described both land use and vegetation type. The land use provided by the Central Geological Survey of the Ministry of Economic Affairs and the vegetation type were retrieved by the Moderate-resolution Imaging Spectroradiometer (MODIS) satellite.
- Vegetation fraction: 10-day vegetation fraction data retrieved from clear-sky observations performed by AVHRR/Metop were provided by the European Organization for the Exploitation of Meteorological Satellites (EUMETSAT) LSA SAF (Satellite Application Facility on Land Surface Analysis). The vegetation fraction corresponds to the complement to unity of the gap fraction at nadir direction, accounting for the amount of vegetation distributed in a horizontal perspective.

Above datasets were interpolated by WPS utility of WRF to a 1-km resolution and Noah MP model grid, as shown in Fig. 2.4.

7

2.1.3 Spin-up-time experiment

When a model is initialized with a different initial state compared to the target place's long-term climatology, the model undertakes a period of spin-up during which its land surface state adjust from the initial conditions to an equilibrium state (Yang et al. 1995a; Shuttleworth et al. 2006). The model output during this adjustment period is highly impacted by the initial condition and consequently may show huge drift render it unusable. Once the model achieves equilibrium, the simulated output usually agrees better with the observations and responds more realistically to the inputs (Ajami et al. 2014; Seck et al. 2015; Brian et al. 2019; Yang et al. 1995a).

This study performed an offline experiment to evaluate the spin-up behavior in the Taiwan region using the Noah MP. The experiment comprised two runs initialized on March 1, 2022, and ended on July 24, 2022, with different initial LSM conditions. The first run, designated as the control run (CTL), was initialized using the CWB High Resolution Land Data Assimilation System (HRLDAS) system (Hung et al., 2014), while the second run applies perturbations (PER) using the monthly mean of March from the first run, which deviates substantially from the real condition.

2.1.4 LSM Sensitivity experiment

Based on the offline experiment structure, Li et al. (2020) quantified the contributions of errors in model structure and parameters in the Noah MP for worldwide sites. The results revealed that five physical processes, including the surface exchange coefficient, SM factor for stomatal resistance, radiation transfer, runoff and groundwater, and surface resistance to evaporation, significantly influenced model performance. Chang et al. (2020) evaluated the sensitivity of Noah MP physical processes at a single site in subtropical forest areas in South China. The most sensitive factors are SM factor for stomatal resistance, canopy stomatal resistance, surface layer exchange coefficient, dynamic vegetation, radiation transfer, and runoff and groundwater. In contrast, six other processes have little or no effect on heat simulation.

This study aimed to assess the sensitivity of Noah MP options to ensemble

spread and develop an effective multi-model LSM perturbation scheme under offline experimental conditions. To accomplish this, five potentially sensitive Noah MP options were selected based on prior research: radiation transfer, surface exchange coefficient, soil-moisture factor controlling stomatal resistance, stomatal resistance, and surface resistance to evaporation and sublimation. A total of 48 combinations from the five physical options corresponded to 48 ensemble members, with details described in Table 2.2.
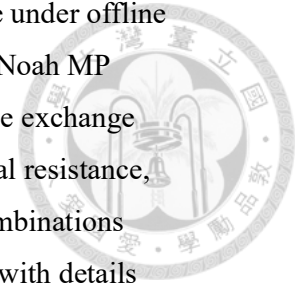
2.1.5 SM and ST equilibrium criteria

The two offline runs described in section 2.2.1 are coupled with identical atmospheric forcing and are anticipated to converge over certain simulation time period. When the two runs approach each other closely, it signifies that the model has reached an equilibrium state, when the memory of LSM initial conditions is minimal. Consequently, it is necessary to establish equilibrium criteria for SM and ST in the experiment, defined as the following:

For SM:

$$|SM_1 - SM_2| < 0.005 \times \min(SM_1, SM_2) \tag{2.1}$$

For ST:

$$|ST_1 - ST_2| < 0.1K \tag{2.2}$$

where SM_1 and SM_2 represent the soil moisture, while ST_1 and ST_2 represent the soil temperature from the two runs.

2.1.6 Option Spread definition

The sensitivity experiment described in section 2.2.2 involves designing a Noah MP ensemble consisting of 48 members. Each member represents a distinct scheme combination of five Noah MP options (Table 2.2). In order to assess the impact of the five Noah MP options on model dispersion, we design a metric termed Option Spread (OS).

9

Here we demonstrate the Option Spread calculation for opt_rad as an example:

1. Opt_rad has three schemes with naming as scheme a, scheme b, and scheme c.
2. For schemes a, b, and c, each scheme is applied by a total of 16 members. Then we calculate the ensemble mean over 16 members for schemes a, b, and c.
3. Option Spread for opt_rad is calculated as the standard deviation of three ensemble mean calculated from step 2.
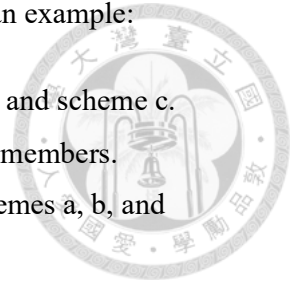
The formula for OS is summarized below:

OS = Standard Deviation(mean(a), mean(b), mean(c), ...)

mean(a), mean(b), mean(c), ... represent the ensemble mean for each scheme within the option.

The larger Option Spread indicates that applying different schemes of the option may produce more dispersive result.

2.2 WRF ensemble experiment

The results from the offline experiments were further examined with a high-resolution ensemble prediction system, the Advanced Research WRF (WRF-ARW) model, to investigate the effect of LSM perturbations on afternoon thunderstorm prediction in Taiwan. The WRF simulations applied three nested domains (Fig. 2.3) with horizontal resolutions of 15 (662×386), 3 (1161×676), and 1 km (799×919), and 52 eta levels up to 20 hPa. We employed a one-way nested run, which disabled feedback from the inner domain to the coarse domain. The physics parameterization schemes included the Yonsei University PBL Scheme (Hong, Noh, and Dudhia 2006), the Goddard microphysics scheme (Tao et al. 2016), the RRTMG shortwave and longwave schemes (Iacono et al. 2008), and the Noah MP LSM (Niu et al. 2011).

Two ensemble experiments were conducted (details summarized in Table 2.3): (1) Experiment only considered initial condition perturbation (ICP), and (2) Experiment included LSM perturbation in addition to the initial condition perturbation (LSMP). In ICP, we initialized 24 ensemble members using the WRFDA Random-CV

10

tool (Barker 2005), with the background based on the initial condition from CWBWRF. The initial conditions of the 3- and 1-km domains were downscaled from the 15-km domain, but high-resolution static data were still applied in both domains (Fig. 2.5a).
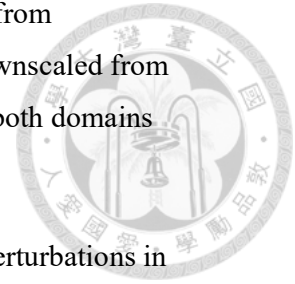
In the LSMP experiment, we applied the Noah MP multi-model perturbations in the 1-km domain using 24 configurations (Table 2.4). The LSM initial condition of each member was obtained from its offline spinning-up run lasting at least three months (Fig. 2.5b). In both experiments, the boundary conditions for the 15-km domain were obtained from the NCEP Global Forecast System (GFS).

2.2.1 Surface verification

A total of 331 surface stations across Taiwan island were used, including 32 conventional weather stations and 299 Automated Weather Stations (AWS). Surface variables included wind speed, wind direction, temperature, surface pressure, and relative humidity. Stations were excluded if they had an elevation difference larger than 150 meters from the closest model grid, if the closest model grid belonged to the ocean, or if the data completeness percentage was below 33%. In order to verify the ensemble prediction result, the root-mean-square error (RMSE) and mean error (ME) were computed against surface observations.

11

Table 2.1 Noah MP tunable options (version 4.3).

Option name	Physical processes
OPT_DVEG	Dynamic vegetation
OPT_CRS	Canopy stomatal resistance
OPT_BTR	Soil moisture factor for stomatal resistance
OPT_RUN	Runoff and groundwater
OPT_SFC	Surface layer drag coefficient
OPT_FRZ	Supercooled liquid water
OPT_INF	Frozen soil permeability
OPT_RAD	Radiation transfer
OPT_ALB	Snow surface albedo
OPT_SNF	Partitioning precipitation into rainfall and snowfall
OPT_TBOT	Lower boundary condition of soil temperature
OPT_STC	Snow/soil temperature time scheme
OPT_RSF	Surface resistance to evaporation and sublimation
OPT_SOIL	Defining soil properties
OPT_PEDO	Pedotransfer functions
OPT_CROP	Crop model
OPT_IRR	Irrigation
OPT_IRRM	Irrigation method
OPT_INFDV	Infiltration in dynamic VIC runoff scheme

Table 2.2 Noah MP options and physical processes used in offline sensitivity experiments.

Option	Physical Processes	Option schemes
OPT_CRS	Canopy stomatal resistance	1. Ball-Berry scheme 2. Jarvis scheme
OPT_BTR	Soil moisture factor for stomatal resistance	1. Noah type 2. CLM type
OPT_SFC	Surface layer exchange coefficients	1. Monin-Obukhov scheme 2. The Noah type
OPT_RAD	Canopy radiation geometry	1. Canopy gaps from 3-D structure and solar zenith angle 2. No canopy gap 3. Gaps from vegetated fraction
OPT_RSF	Surface resistant to evaporation/sublimation	1. Sakaguchi and Zeng's scheme 2. Sellers's scheme

Table 2.3 Perturbations design in two ensemble experiments.

21

Exp.	Perturbations		
	Atmospheric IC	**LSM multi-model**	**LSM IC**
ICP	✔		
LSMP	✔	✔	✔

Table 2.4 Noah MP options involved in LSM perturbation of LSMP.

Option name	Physical Processes	Option schemes	
OPT_CRS	Canopy stomatal resistance	a.	Ball-Berry scheme
		b.	Jarvis scheme
OPT_SFC	Surface layer exchange coefficients	a.	Monin-Obukhov scheme
		b.	The Noah type
OPT_RAD	Canopy radiation geometry	a.	Canopy gaps from 3-D structure and solar zenith angle
		b.	No canopy gap
		c.	Gaps from vegetated fraction
OPT_RSF	Surface resistent to evaporation/sublimation	a.	Sakaguchi and Zeng's scheme
		b.	Sellers's scheme

14
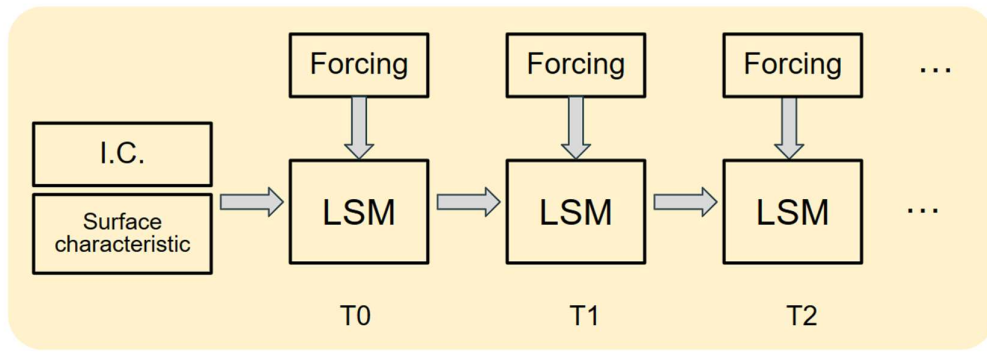
FIG. 2.1 Offline experiments' schematic diagram.
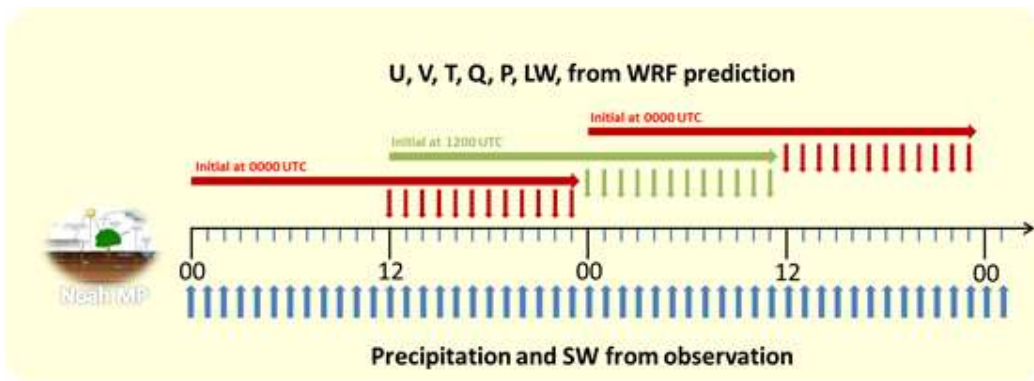
FIG. 2.2 Offline experiment's atmospheric forcing data schematic diagram.
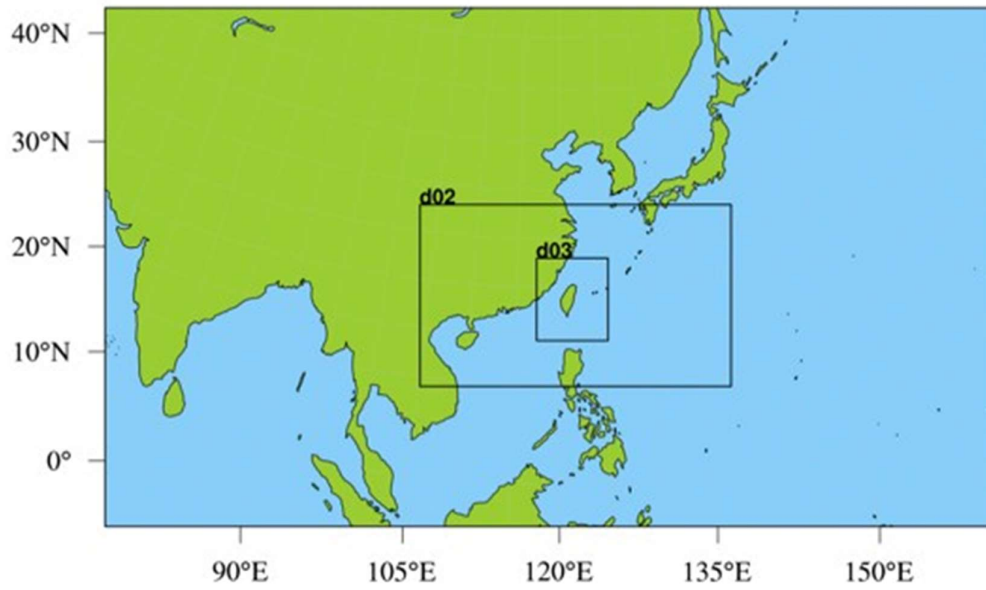
FIG. 2.3 Configuration of 15-km, 3-km, and 1-km computing domains. The offline experiments domain is identical to the 1-km (d03) domain.

(a)

Terrain Height (m)

(b)

Taiwan Land Use Distribution

- Evergreen Needleleaf Forest
- Evergreen Broadleaf Forest
- Deciduous Needleleaf Forest
- Deciduous Broadleaf Forest
- Mixed Forests
- Closed Shrublands
- Open Shrublands
- Woody Savannas
- Savannas
- Grasslands
- Permanent Wetlands
- Croplands
- Urban and Built-Up
- Cropland
- Barren or Sparsely Vegetated

(c)

Vegetation Fraction

(d)

Taiwan Soil Category Distribution

- SAND
- Loamy Sand
- Sandy Loam
- Silt Loam
- Loam
- Sandy Clay Loam
- Silty Clay Loam
- Clay Loam
- Sandy Clay
- Silt Clay
- Clay
- Water

FIG. 2.4 Static data of 1-km resolution in this study. (a) Terrain elevation, (b) Land use, (c) Vegetation fraction, and (d) Soil texture

17

(a)

(b)
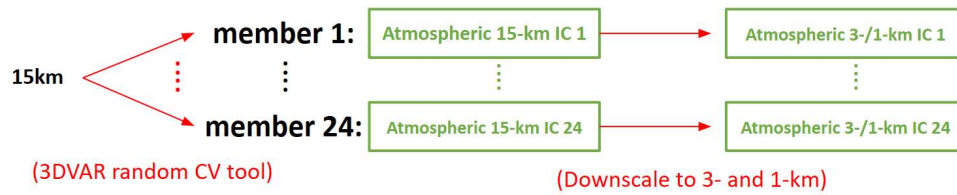
FIG. 2.5 (a) LSM IC perturbation and (b) WRF IC perturbation in ensemble experiment.

3. Offline experiment result

3.1 Offline spin-up Experiment

This study conducted an offline experiment to assess the spin-up behavior of Noah MP across the Taiwan area. The experiment consisted of two runs with distinct initial SM and ST conditions, as detailed in section 2.2.1. Figure 3.1 illustrates the differences in their initial conditions. In terms of SM, the exp_ctrl exhibits a drier pattern in the western region at the first layer and a moister pattern at the fourth layer. As for ST, a cold pattern is observed at the first layer, approaching zero at the fourth layer.

Figure 3.2 shows the time evolution of the spatial average over Taiwan. Inverse phases between SM and ST patterns highlight the precipitation events. We speculate that higher SM from rainfall will decrease ST because of lower solar radiation and the Bowen ratio.

According to the equilibrium criteria defined in section 2.4.1, the results indicate that SM reaches equilibrium in two and a half months for the top three layers, while the fourth layer only takes one and a half months to spin-up fully. Notably, the spin-up time at the fourth layer of SM is shorter than that in the top three layers, which contradicts the conventional understanding of SM spin-up. On the other hand, ST achieves equilibrium from one week to two months as depth increases.

Figures 3.3.a and 3.3.b depict the spatial distribution of spin-up time for SM and ST, respectively. Most of Taiwan requires approximately one month to reach SM equilibrium. Longer time is required for certain place, such as around two months in the southwest region and East Rift Valley, and even up to five months in some urban areas. The pattern of SM spin-up times appears to be associated with land use and soil category distribution; however, further research is needed to explore these relationships. By contrast, ST over most of Taiwan reaches equilibrium within one month; whereas in the northeast and East Rift Valley, it takes one to two months to achieve equilibrium.

This spin-up time to reach the equilibrium state is related to the definition of

equilibrium criteria and may also be influenced by the initial conditions of ST and humidity. However, qualitatively, both experiments have provided sufficient evidence of the required spin-up time to reach the equilibrium. It is noteworthy that our spin-up time is shorter compared to the majority of studies for two reasons. Firstly, our offline experiment was initialized with HRLDAS from CWB, which has been in operation for several years, resulting in the soil variables being initialized at a relatively realistic state. Secondly, our offline experiments experience multiple rainfall events, which typically reduce the spin-up time (Bhattacharya et al. 2018; Rodell et al. 2005).

Considering the spin-up characteristic for SM and ST in four layers, the LSM should reach equilibrium within three months. Therefore, the following analysis, including the offline sensitivity experiment and WRF ensemble experiments, will apply LSM initial conditions after spin-up for at least three months to avoid uncertainty in LSM initial conditions.

3.2 LSM Sensitivity experiment

The offline sensitivity experiment described in section 2.2.2 aims to determine an effective LSM multi-physics perturbation scheme for afternoon thunderstorms ensemble forecast. Consequently, we focus on the atmospheric conditions favoring afternoon thunderstorms. The subsequent analysis period spans from June 21 to July 06, with afternoon thunderstorm events and at least a spin-up period over three months. Figure 3.4 illustrates the daily accumulated precipitation in this period, showing active afternoon thunderstorms, particularly over the western Taiwan. Our analysis focuses on sensible and latent heat flux because they are the most critical variables determining the impact of the land surface on the atmosphere.

Figure 3.4 reveals a significant occurrence of rainfall events throughout the experimental periods. However, it is well known that precipitation and shortwave radiation dominated the land surface states and subsequent land surface processes. We are particularly interested in investigating the impact of dry and wet weather conditions on the uncertainty of Noah MP. Therefore, we carried out an additional **NORAIN** experiment. In this experiment, the atmospheric forcing data is modified by setting rainfall to zero and adjusting the downward solar radiation to clear sky

20

conditions over throughout the experiment period. This **NORAIN** experiment will be compared with the unmodified experiment (**CTRL)** in the subsequent discussions.

Figure 3.5 depicts the spatial distribution of OS after temporal averaging from June 21 to July 06 for sensible and latent heat flux. In terms of both sensible and latent heat flux, opt_sfc exhibits the highest OS, while opt_btr demonstrates the lowest OS across Taiwan. Notably, a contrasting pattern emerges between the mountainous and plain regions. For opt_crs and opr_rsf, the OS is higher in the plain area and lower in the mountain area, whereas opt_sfc demonstrates higher values in the mountain area and lower values in the plain area, suggesting different sensitivity to the physical processes across the mountainous and plain regions. The possible physical explanation for such variability is the processes' common association with vegetation cover: opt_crs and opt_btr determine the canopy transpiration; opt_sfc dominates the sensible heat from the surface, which is also influenced by vegetation height; opt_rad is related to the parameterization of short wave radiation absorbed by vegetation layer.

Figure 3.6 and 3.7 displays the average diurnal cycle of OS for elevations below 300 m. The results of three more dispersive options, including opt_sfc, opt_rad, and opt_crs demonstrated a pronounced diurnal pattern in OS, with values increasing in the morning and decreasing in the evening.

For the latent heat flux, the most sensitive option is opt_crs, aligning with the results presented in Fig. 3.5, while the least sensitive option is opt_btr. Concerning the sensible heat flux, opt_sfc exhibits the highest increase in OS, whereas opt_btr and opt_rsf display relatively lower OS values.

Figure 3.7 depicts the diurnal cycle of OS for elevations above 300 m. The daily patterns exhibit similarities to the results for elevations below 300 m, with opt_sfc consistently displaying significantly higher values. The opt_sfc is related to the sensible heat flux coefficient, and one of the main differences between the two schemes in opt_sfc is the canopy height consideration, which may result in a higher spread in the forest region, namely the higher altitude area. More details of the role of canopy height in opt_sfc are presented in the Discussion section.

Generally, **NORAIN** experiment gets a higher OS than **CTRL**, especially in sensible heat flux. There are two possible reasons. Firstly, **NORAIN** experiment has higher solar radiation and higher energy absorbed by the land surface, resulting in more dispersal of the LSM ensemble during daytime, especially with opt_sfc which determined the sensible heat flux. Secondly, the **CTRL** experiment receives more precipitation, resulting in higher SM. Supposedly, SM lowers the proportion of sensible heat flux and thus decreases its uncertainty.

The sensitivity experiment results are summarized in Table 3.1. Based on the ranking of the OS, the four most sensitive options are selected to compose the LSM perturbations, namely the opt_sfc, opt_rad, opt_crs, and opt_rsf, in the following ensemble experiments.

22

Table 3.1 The summarized table of sensitivity for five options. With a normalize scale of 1 to 5, A higher value means more sensitive.
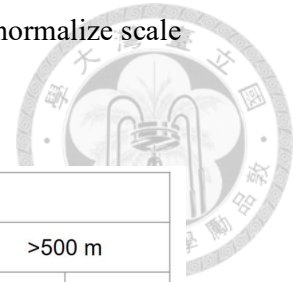
	norain				ctrl			
	<500 m		>500 m		<500 m		>500 m	
	LH	SH	LH	SH	LH	SH	LH	SH
OPT_CRS	5	3	3	3	3	3	3	3
OPT_BTR	1	1	1	1	1	1	1	1
OPT_SFC	4	5	5	5	4	5	5	5
OPT_RAD	4	4	4	4	4	4	4	4
OPT_RSF	2	2	2	1	2	2	1	1
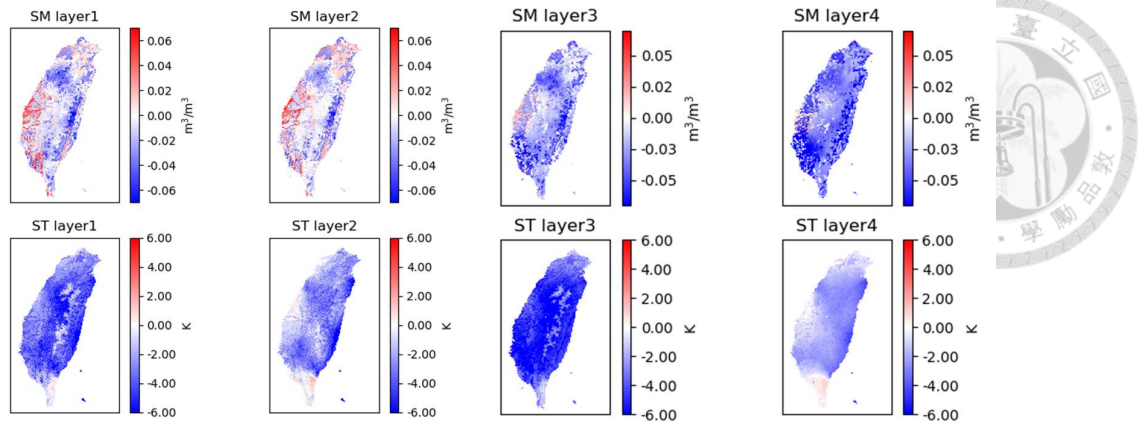
FIG. 3.1 Initial difference of the soil moisture and soil temperature across four layers in the two spin-up runs.
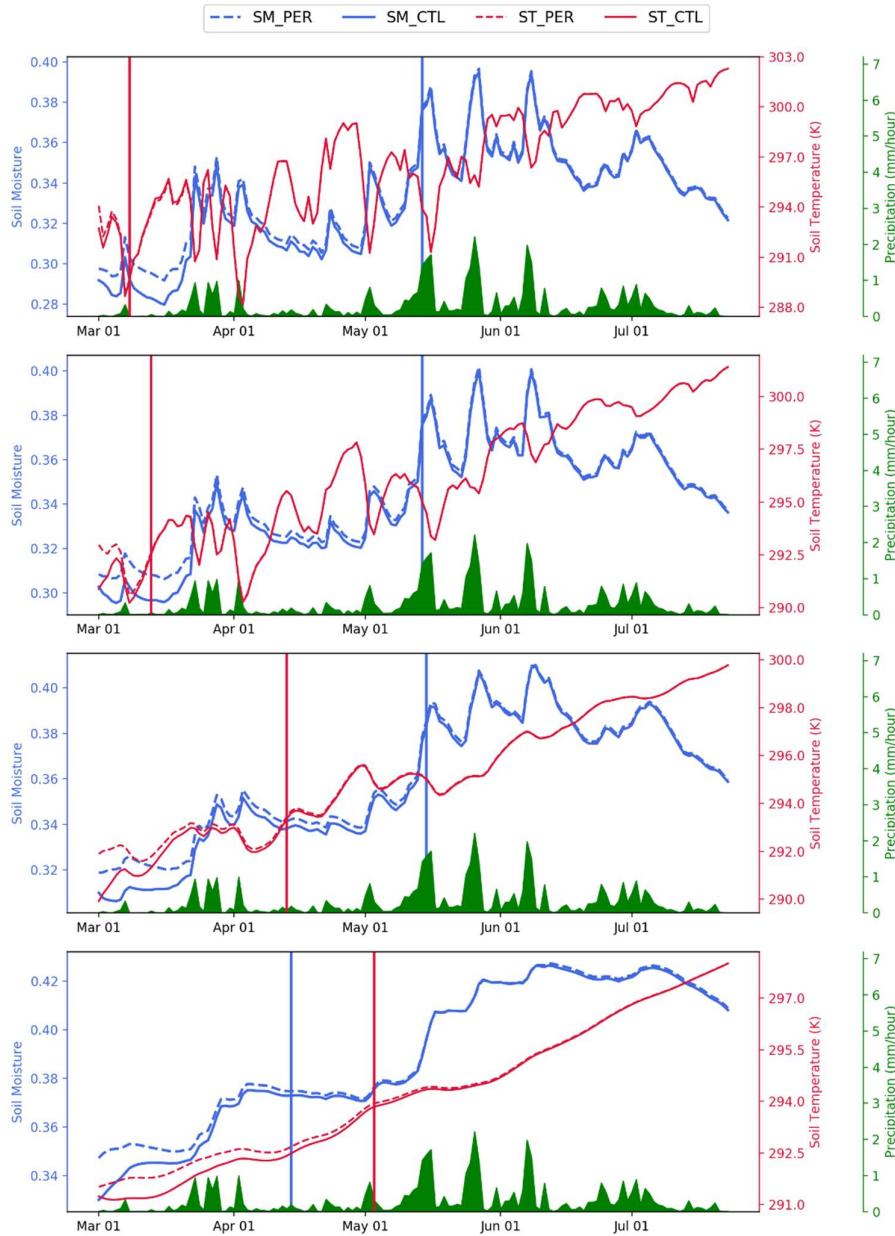
FIG. 3.2 Time series of precipitation and the soil variables across four layers in the offline spin-up experiment. The blue line, red line, and green area represent the soil moisture, soil temperature, and precipitation, respectively. The solid lines represent the exp_ctl; The dashed lines represent exp_per. The vertical lines represent the date on which the experiment reaches equilibrium criteria.

25
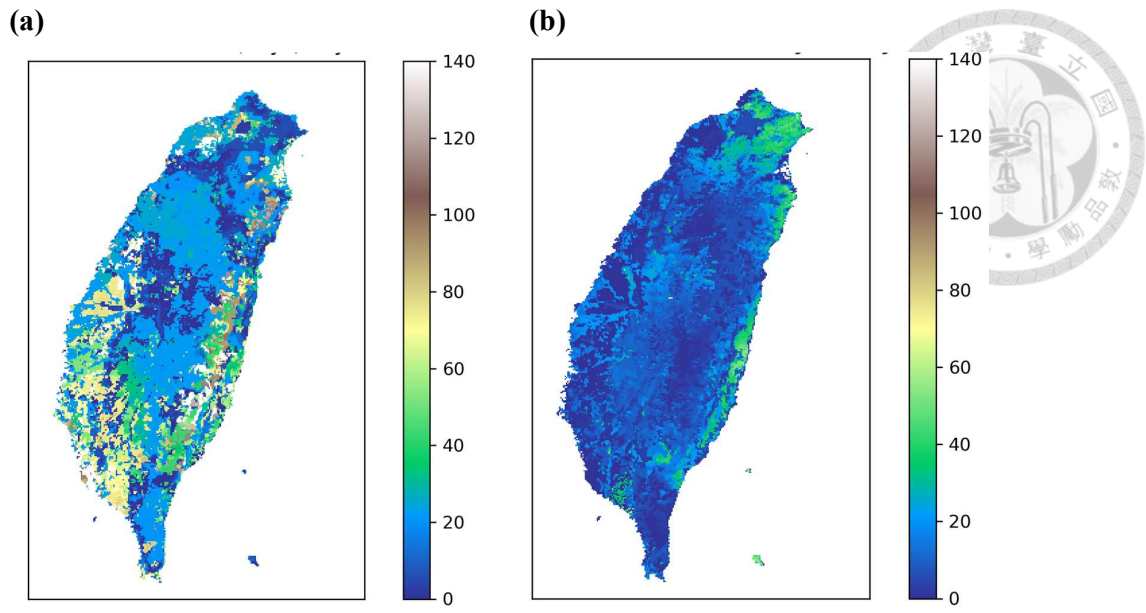
FIG. 3.3 Spatial distribution of spin-up time (days) for (a) soil moisture and (b) soil temperature at the first layer.
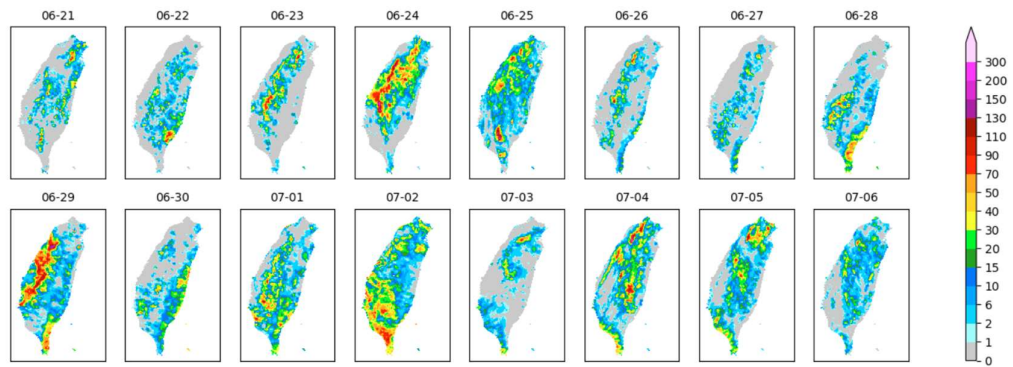
FIG. 3.4 Daily accumulated rainfall of the analytical period.
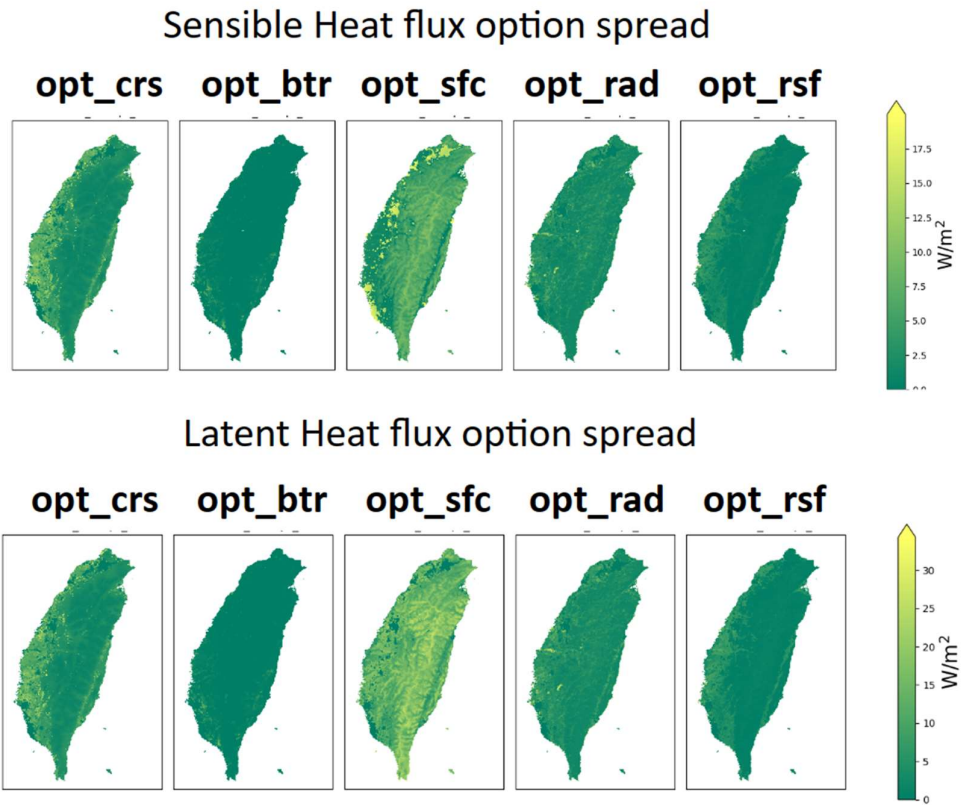
FIG. 3.5 Option Spread's spatial distribution of five options for latent heat flux and sensible heat flux.

(a)
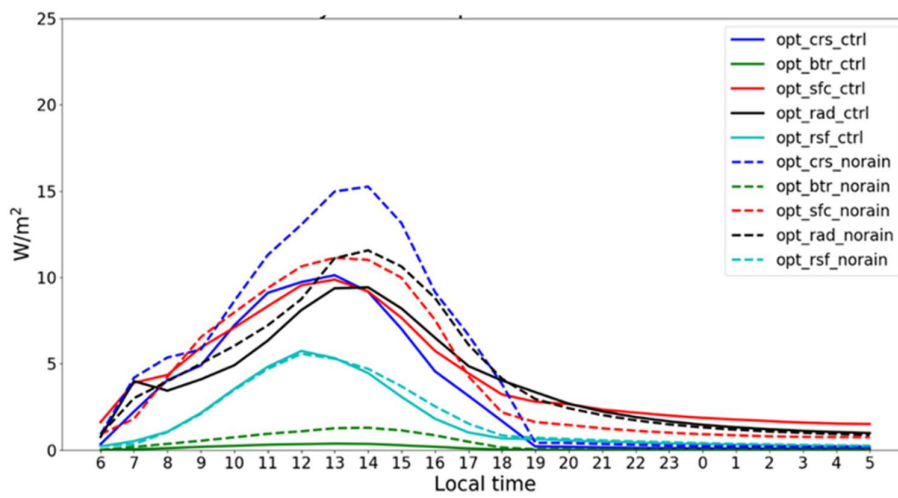
(b)
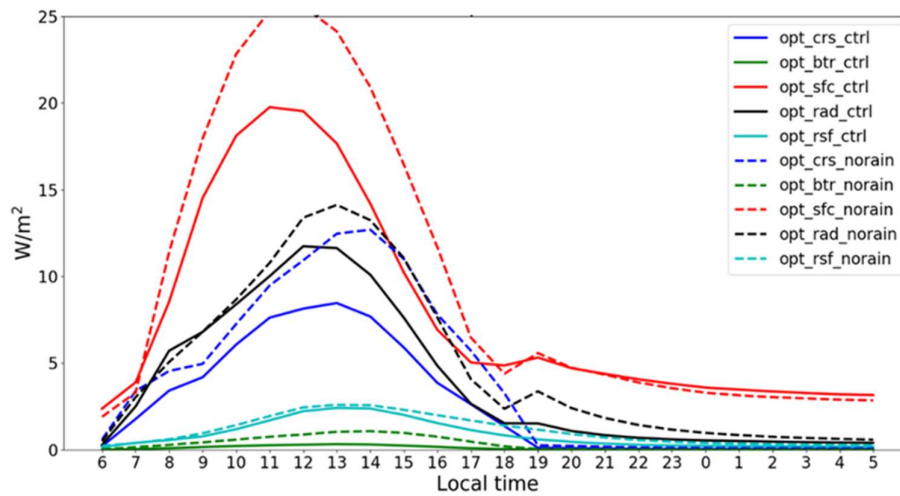
FIG. 3.6 The diurnal cycle of the average OS for elevations below 300 m, where (a) is for latent heat flux and (b) is for sensible heat flux. Colors represent five options; solid lines describe the CTRL experiment, dashed lines represent the NORAIN experiments.
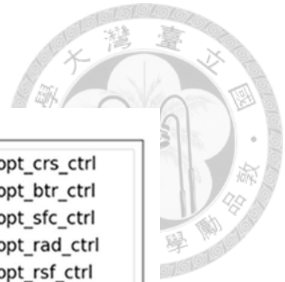
(a)
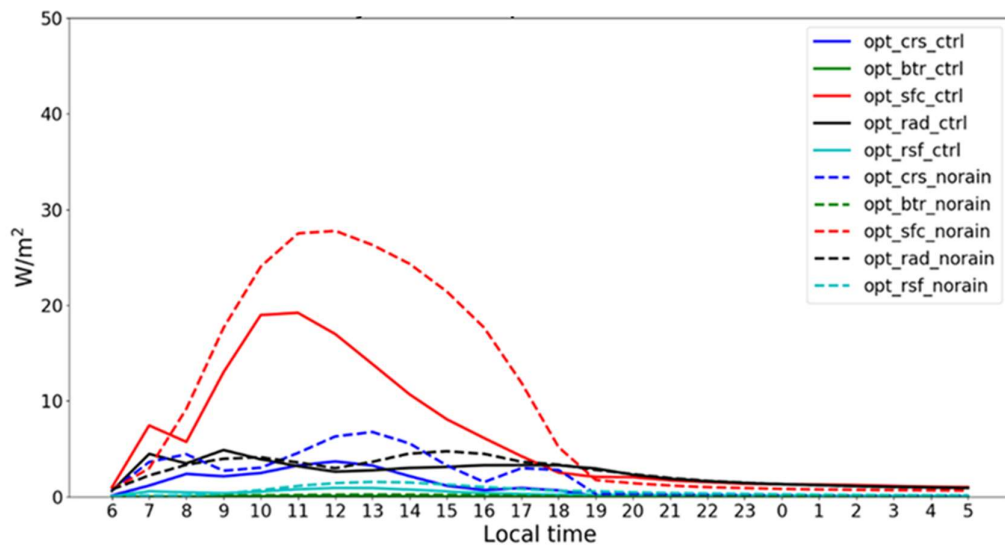
(b)
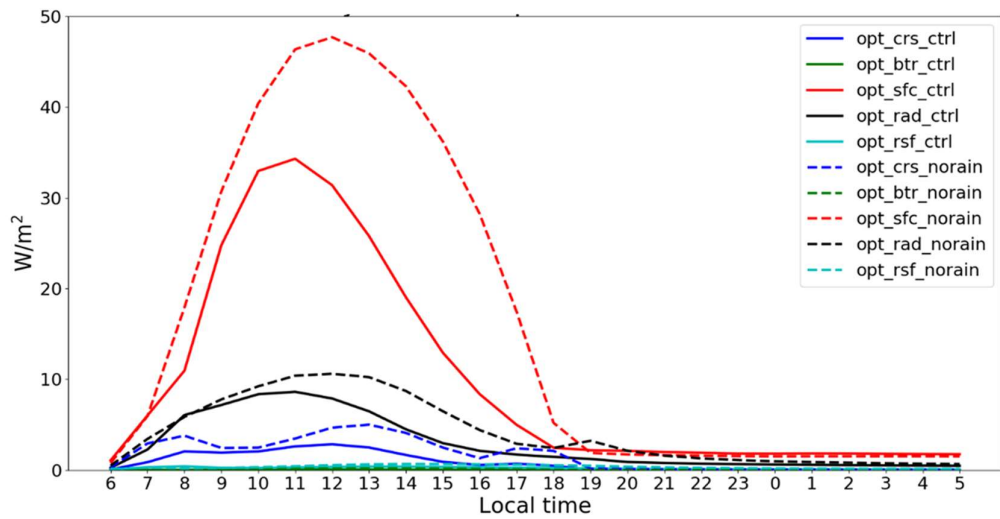
FIG. 3.7 Same as Fig. 3.6, but for elevations above 300 m.

4. WRF ensemble experiment result
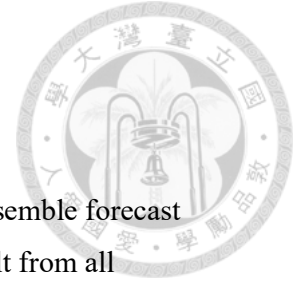
4.1 Cases analysis

The role of LSM perturbation in the afternoon thunderstorm ensemble forecast is examined firstly with the case on June 24, 2022. The composite result from all cases will be presented next.

The entire experimental period can be divided into three distinct phases. The first phase occurred from 20:00 on June 23 LST to 08:00 on June 24 LST, representing a stable nocturnal boundary layer condition and is referred to as the **stable nocturnal phase**. During this phase, Taiwan experiences a relatively stable atmospheric state characterized by low convective activity. The second phase spans from 08:00 to 13:00 on June 24 LST and is called the **pre-storm phase**, representing the cook-up period for the afternoon thunderstorm. This phase is of particular interest as it provides insights into the pre-storm environment and sets the stage for convective development. The third period, from 13:00 to 20:00 on June 24 LST, corresponds to the occurrence of the afternoon thunderstorm and is referred to as the **convection phase**. During this phase, the convective processes intensify, leading to significant changes in atmospheric conditions.

Figure 4.1 displays the daily accumulated rainfall from ICP and LSMP experiments, including 24 ensemble members each and observations. The simulation results indicate a similarity in rainfall spatial patterns between the simulations and observation. However, all ensemble members underestimate the extreme rainfall in the central Taiwan region. A comparison between ICP and LSMP reveals slight differences among the ensemble members.

Figures 4.2 to 4.8 show the boxplot of diurnal variation in key physical parameters averaged over grids with elevations below 300 m, except that precipitation is calculated for all model grids over the land. Particular attention will be paid to temporal variations in these boxplots.

Figure 4.2 reveals notable differences between the model and observation results. The model's prediction of rainfall begins at 13:00 LST, whereas the observed

rainfall starts two hours later at 15:00 LST, indicating that the model's timing of precipitation is too early. Moreover, the model's precipitation peak also occurs prematurely and also presents an underestimation of the peak values. When comparing the two model experiments, their medians are more or less similar; however, the LSMP experiment exhibited more extensive spreads, which grow with time after sunrise until the early afternoon. These findings suggest that the LSMP perturbation substantially impacts precipitation, highlighting the need to consider LSM perturbation during the pre-storm phase of afternoon thunderstorms. Consequently, the subsequent analysis primarily focuses on near-surface variables in the pre-storm environment.

The diurnal cycle of sensible heat flux shown in Fig. 4.3 illustrates a simultaneous increase from 07:00 LST in both experiments. The medians at each hour are slightly larger in ICP than in LSMP, indicating that ICP produces a high sensible heat flux from the surface to the atmosphere. As for the spread, LSMP has a significantly higher spread all day long. It increases during the pre-storm phase and gradually decreases in the convection phase.

Figures 4.4, 4.5, and 4.6 depict the diurnal cycle of 2-m temperature, PBLH, and ground temperature. In the pre-storm phase, the median of 2-m temperature and PBLH in the ICP experiment is higher than those in the LSMP experiment, while the ground temperature is lower in the ICP experiment. These results align with the energy perspective, indicating that our ensemble results of heat flux and thermal variables are consistent with physical expectations.

Fig. 4.7 illustrates the diurnal cycle of latent heat flux. ICP has lower medians in latent heat flux than LSMP before 9:00 LST but higher after 11:00 LST. By contrast, Fig. 4.8 reveals that the 2-m water vapor for ICP becomes higher at 10:00 LST, indicating that the near-surface water vapor is not solely determined by latent heat flux. Additionally, Fig. 4.9 demonstrates that ICP exhibits higher wind speeds soon after the pre-storm phase begins, suggesting that advection may play a role in the changes of near-surface water vapor. Fig. 4.10 (a) displays the spatial distribution of wind components and the 2-m temperature difference between the two experiments (ICP-LSMP) at 10:00 LST. These results generally align with the previous findings

that ICP has a higher 2-m temperature in the lower altitude region. Higher land temperature anomalies may induce higher in-land wind components and moisture advection. Figure 4.10 (b) presents the spatial distribution of differences in 10-m wind and 2-m water vapor. It can be observed that in the low-altitude regions, higher in-land wind components are accompanied by higher 2-m water vapor. In summary, the higher sensible heat flux in ICP leads to higher temperatures in the lower boundary layer and ground temperatures. This induces stronger in-land winds associated with higher 2-m water vapor in the lower altitude region.

The verification of surface variables is presented in Figs. 4.11 to 4.13. Figure 4.11 shows that LSMP exhibits higher temperature spreads in the pre-storm phase than ICP, with the latter approaching zero in the pre-storm phase. Additionally, the RMSE for LSMP slightly increases, possibly due to higher mean errors. The water vapor verification (Fig. 4.12) indicates that LSMP has a larger spread and underestimates the water vapor, representing lower RMSE during the pre-storm phase. Figure 4.13 demonstrates minimal differences in wind speed between the two experiments. However, it is worth noting that LSMP exhibits a higher spread and lower RMSE in this particular case.

Studies have shown that ensemble systems with multi-physics designs often display characteristics of classification among their ensemble members (Li and Hong, 2014). In order to investigate this phenomenon, we conducted a verification analysis was conducted to determine if distinct classifications exist within the ensemble results. Figure 4.11 presents a 2-m water vapor heat map illustrating the inter-member differences observed in the experiment. Interestingly, fFor the ICP, the inter-member differences appear to be relatively minor and homogeneous. However, within the LSMP, two distinct groups can be identified. These groups correspond to the use of different opt_sfc options, specifically the Noah type and M-O scheme, respectively. This finding suggests that opt_sfc exhibits a greater sensitivity in this particular case, and further discussions of opt_sfc sensitivity are presented in the Discussion section.

4.2 Composite result

To ensure the robustness of our findings, we extend our ensemble experiment

to include four additional afternoon thunderstorm cases: June 25, 2022, June 29, 2022, July 04, 2022, and July 20 2022. The composite result of these five cases is evaluated by representing the ensemble outcomes using boxplots, as described in Section 4.1. By considering the collective information from these five cases, we aim to develop an overarching conceptual model that can effectively elucidate the impact of LSM-based perturbation scheme on the ensemble forecast of afternoon thunderstorms.

The composite results indicate that the sensible, latent, and ground heat flux exhibit relatively lower variability during the stable nocturnal phase. However, as the pre-storm phase commences, the variability of these variables increases. This heightened variability indicates the dynamic nature of the atmospheric conditions during this phase. Interestingly, during the convection phase, both the spread and median of LSMP and ICP variables decrease, suggesting a convergence of these variables.

When examining the energy balance of the ensemble mean during the pre-storm phase, it is evident that LSMP demonstrates lower latent and sensible heat fluxes, accompanied by higher ground heat flux and ground temperature, as illustrated in Figure 4.13 and 4.14. This finding suggests that in the case of LSMP, more energy is stored on the land surface instead of transported into the atmosphere, resulting in higher ground temperature and higher ground heat flux. The phenomenon is related to the sensible heat exchange coefficient determined by opt_sfc. The coefficient is lesser in LSMP, consistent with the lower sensible heat flux results. The planetary boundary layer height (PBLH) and 2-m temperature also revealed higher values in the ICP experiment, correspond well to its higher sensible heat flux.

When examining the moisture budget, it is apparent that LSMP exhibits higher water vapor levels at the 2-m height (Fig. 4.15a) during the stable nocturnal phase. However, as the pre-storm phase commences, the values in ICP surpasses LSMP at 10:00 LST. This excess water vapor in ICP cannot be solely attributed to a higher latent heat flux (Fig. 4.15b), as the latent heat flux of ICP exceeds LSMP only after 11:00 LST. It suggests that horizontal advection of water vapor plays a significant role. The wind speed analysis (Fig. 4.15c) further supports this finding, indicating that ICP experiences higher wind speeds than LSMP during the pre-storm phase, as

33

observed on June 24, 2022.

      Finally, we have summarized a possible conceptual model is summarized based on our the above findings. Firstly, we have identified that the opt_sfc parameter in the Noah MP scheme is identified as the most sensitive factor in our study, as it determines the exchange coefficient for sensible heat flux. Consequently, LSMP exhibits a wider range of spread in sensible heat flux and a lower ensemble mean compared to ICP. This lower sensible heat flux results in lower planetary boundary layer height (PBLH) and 2-meter temperature but higher ground temperature. The decrease in atmospheric temperature leads to higher inland wind components, which further reduces the amount of water vapor in LSMP.
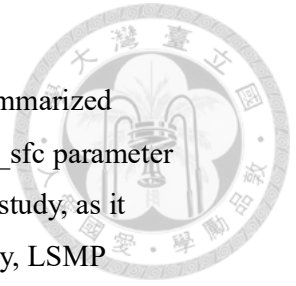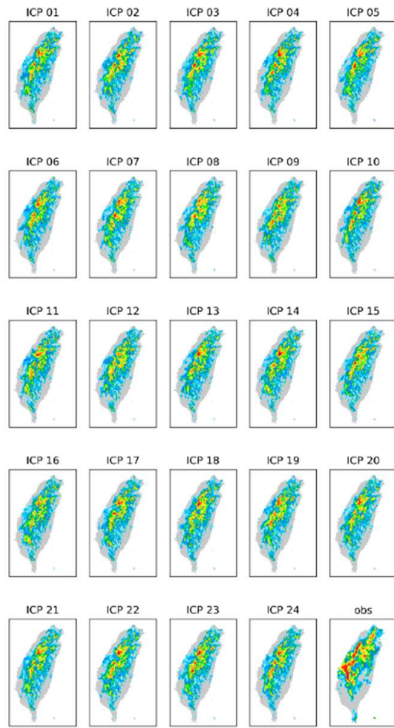
(a) **(b)**
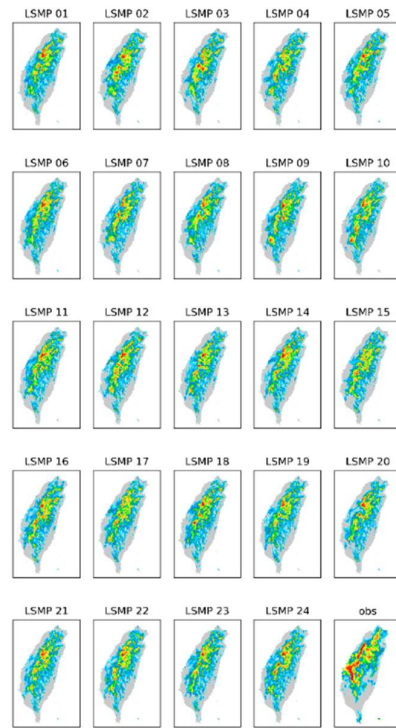
FIG. 4.1 The daily accumulated precipitation for 24 members of (a) ICP and (b) LSMP from 20:00, June 23 LST to 20:00, June 24 LST. The figure in the bottom right corner is observations.
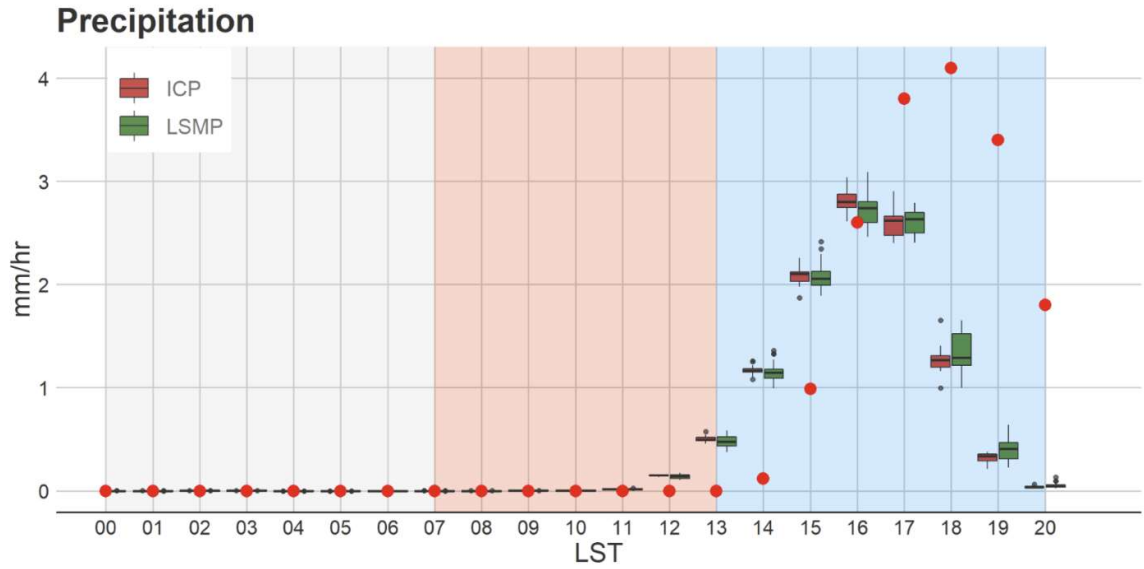
FIG. 4.2 The diurnal cycle of the spatial average of precipitation. The red and green boxplot represents ensemble distribution for ICP and LSMP, respectively. The red dot represents QPESUMS observation. The three colored regions represent indicate the stable nocturnal phase, pre-storm phase, and convection phase.
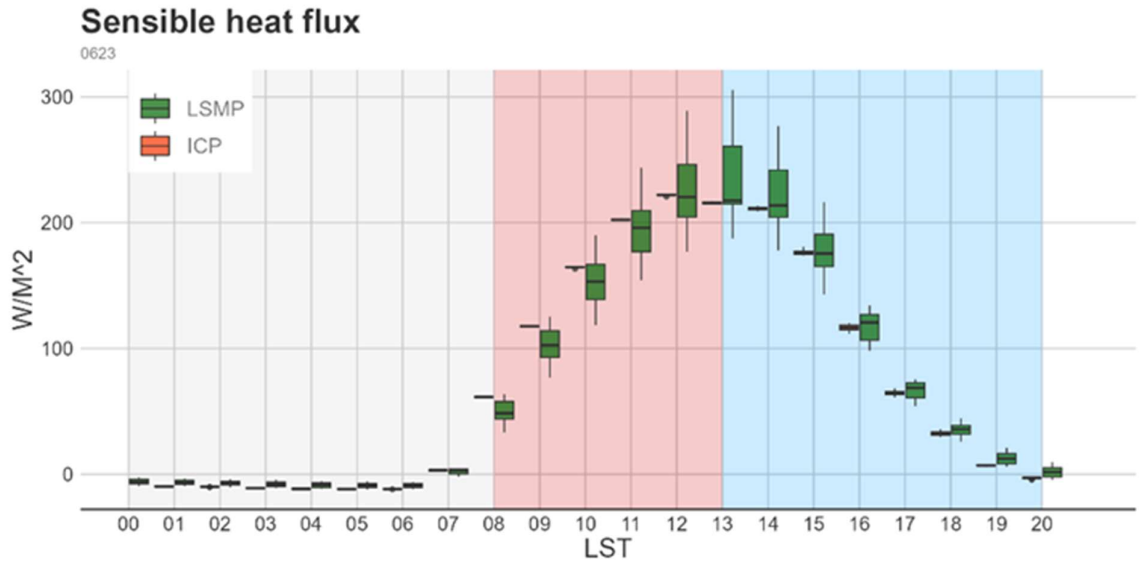
FIG. 4.3 The same as Fig. 4.2, but for sensible heat flux with terrain elevation below 300 m.

36
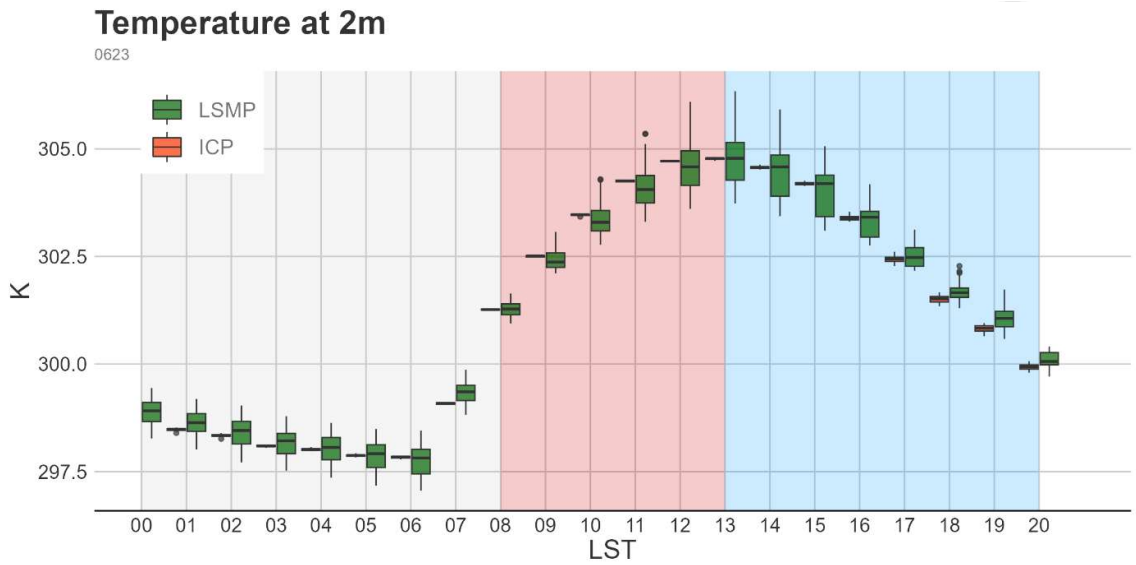
FIG. 4.4 The same as Fig. 4.2, but for the 2-m temperature below 300 m elevation.
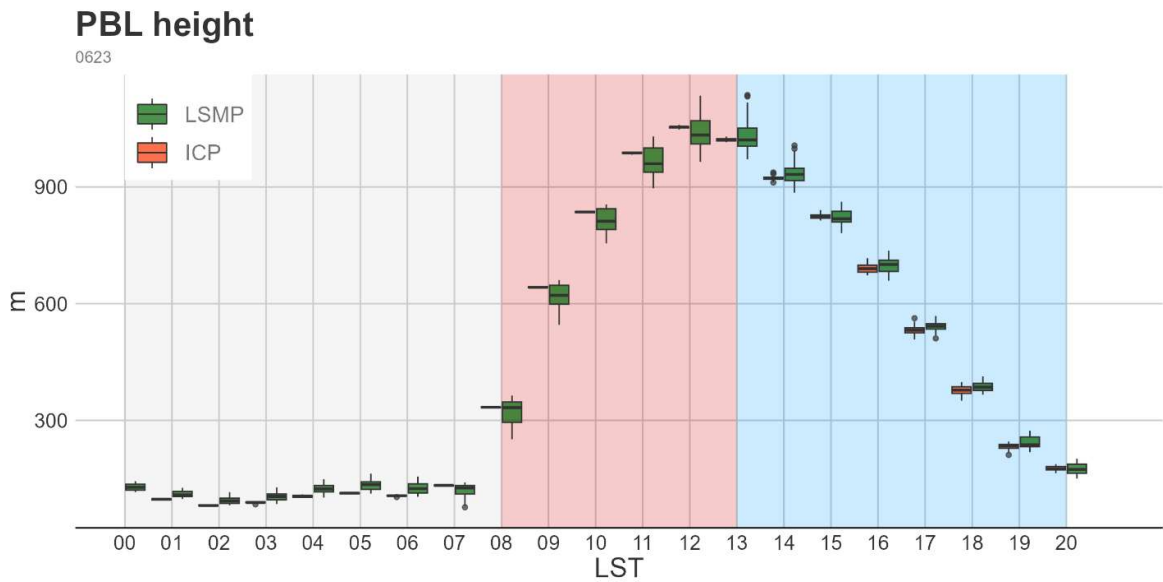
FIG. 4.5 The same as Fig. 4.2, but for planetary boundary height for terrain below

300 m elevation.
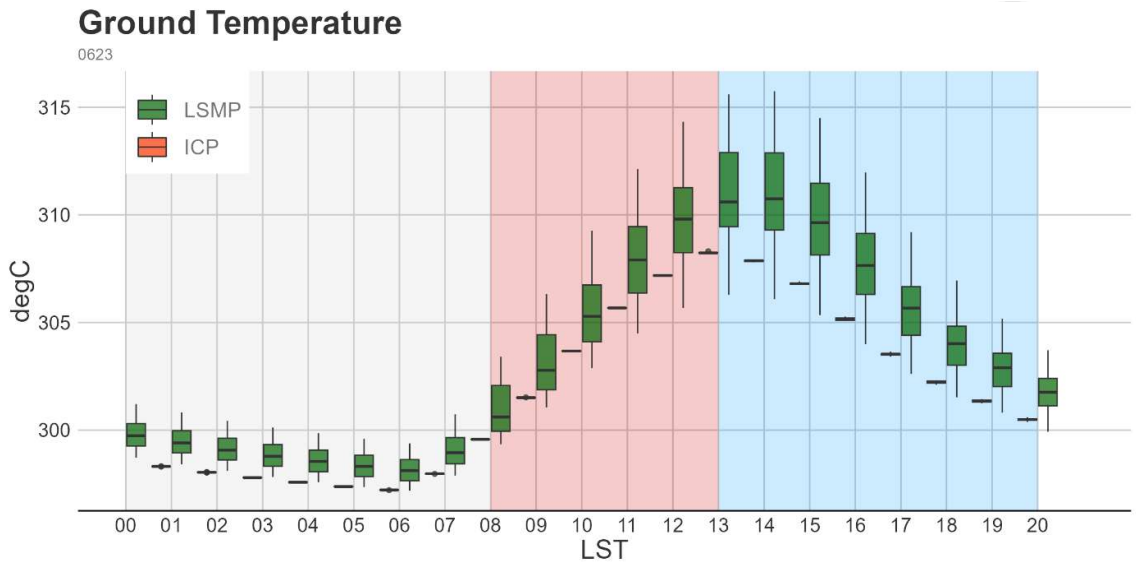
FIG. 4.6 The same as Fig. 4.2, but for ground temperature at terrain heights below 300 m.
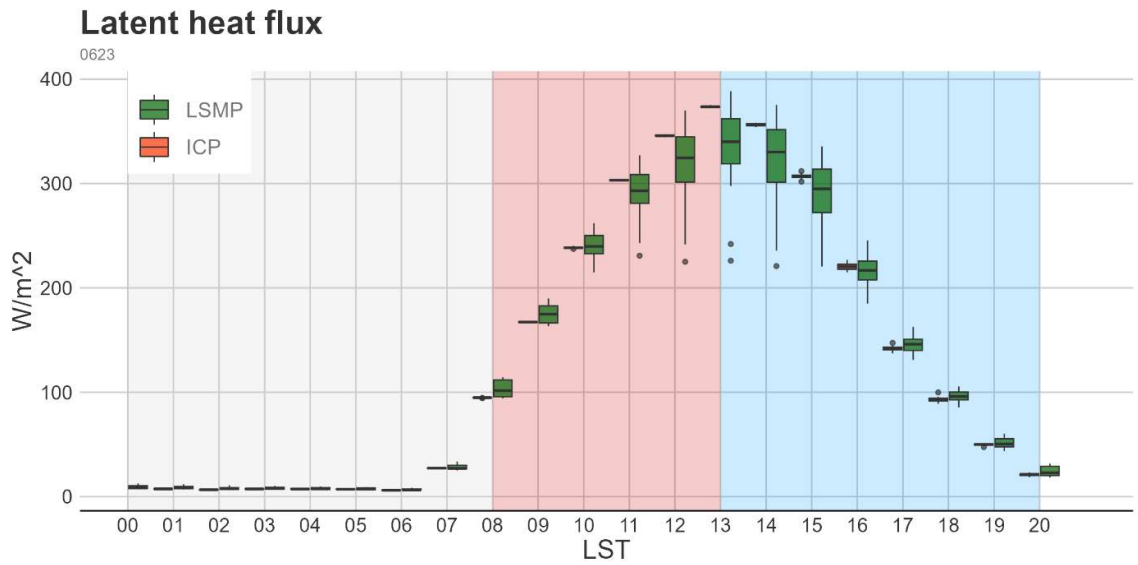
FIG. 4.7 The same as Fig. 4.2, but for latent heat flux where terrain heights are below 300 m.
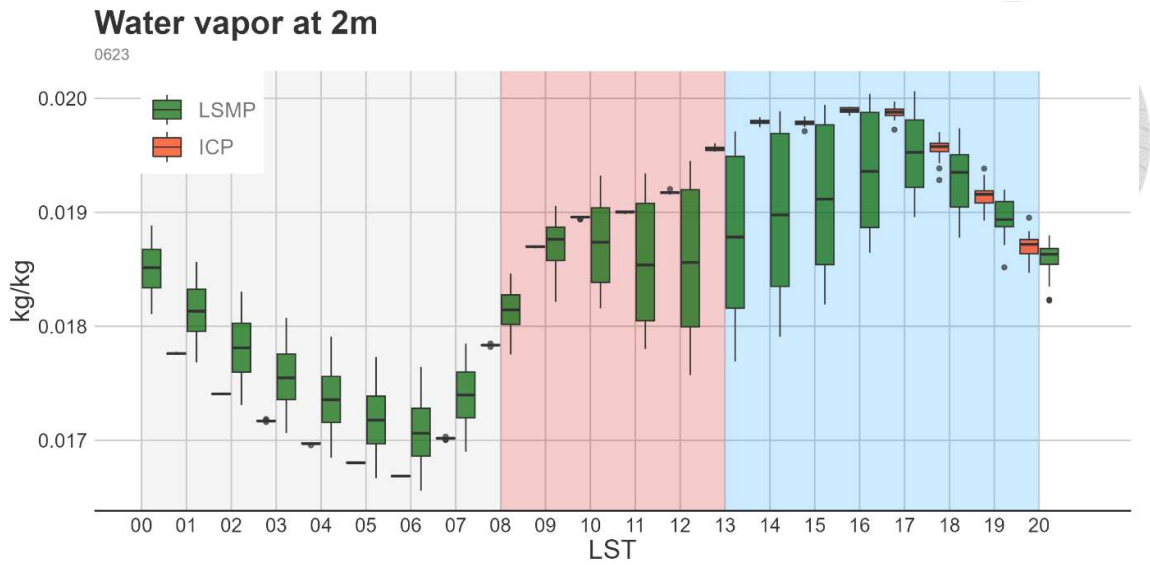
Water vapor at 2m

FIG. 4.8 The same as Fig. 4.2, but for 2-m water vapor where terrain heights are below 300 m.
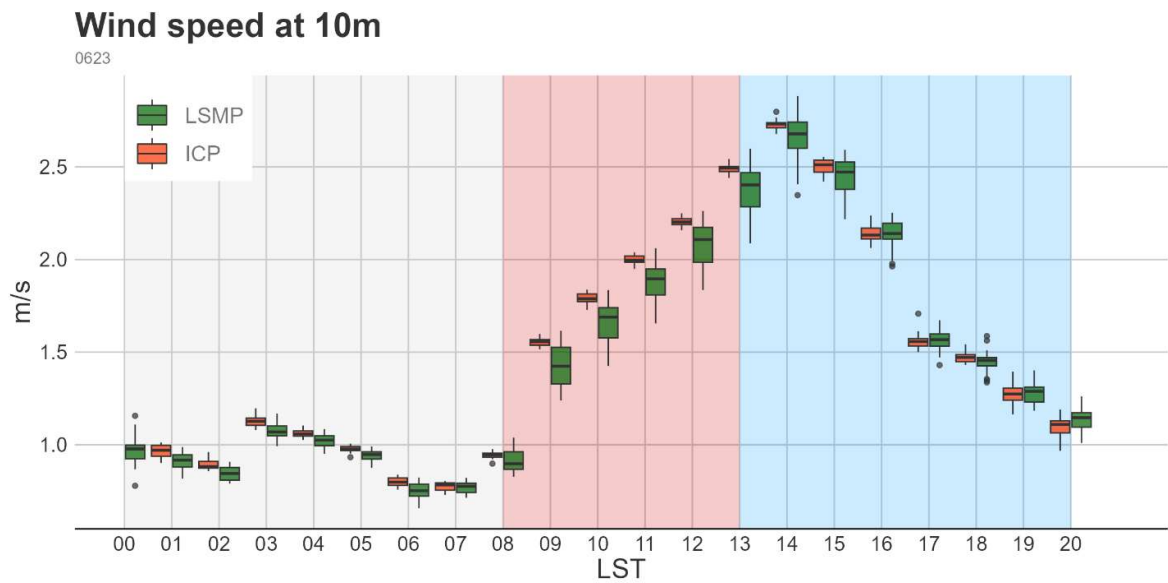
Wind speed at 10m

FIG. 4.9 The same as Fig. 4.2, but for wind speed at 10-m height where terrain heights are below 300 m.

(a)

Wind and T2 diff (ICP-LSMP)

(b)

Wind and Q2 diff (ICP-LSMP)
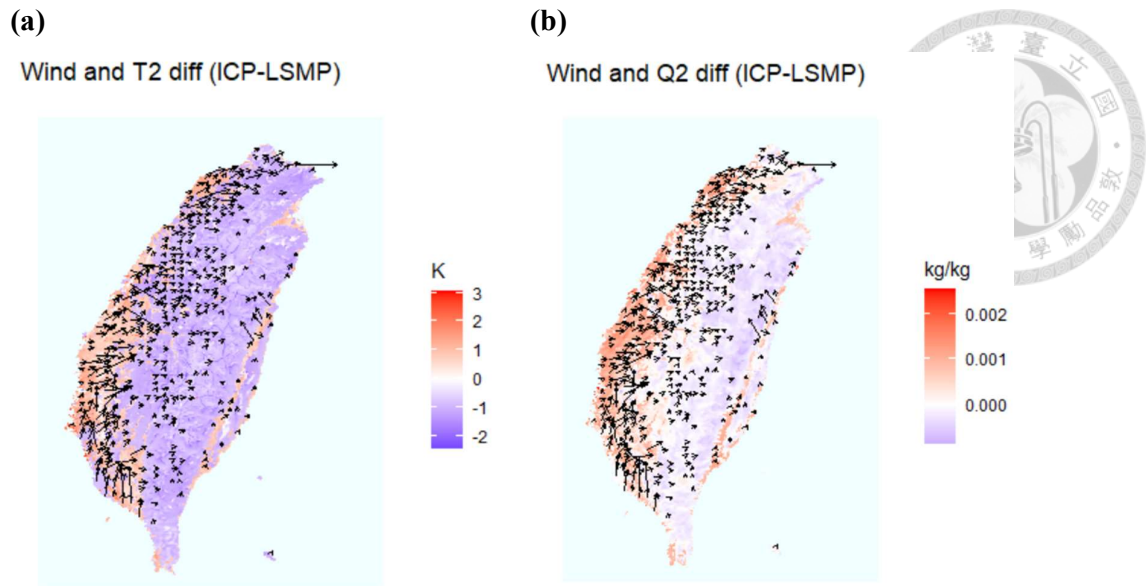
FIG. 4.10 The spatial distribution at 10:00 LST for **(a)** differences in 2-m wind and temperature, and **(b)** differences in 2-m winds and water vapor between ICP and LSMP

(a)

(b)

(c)
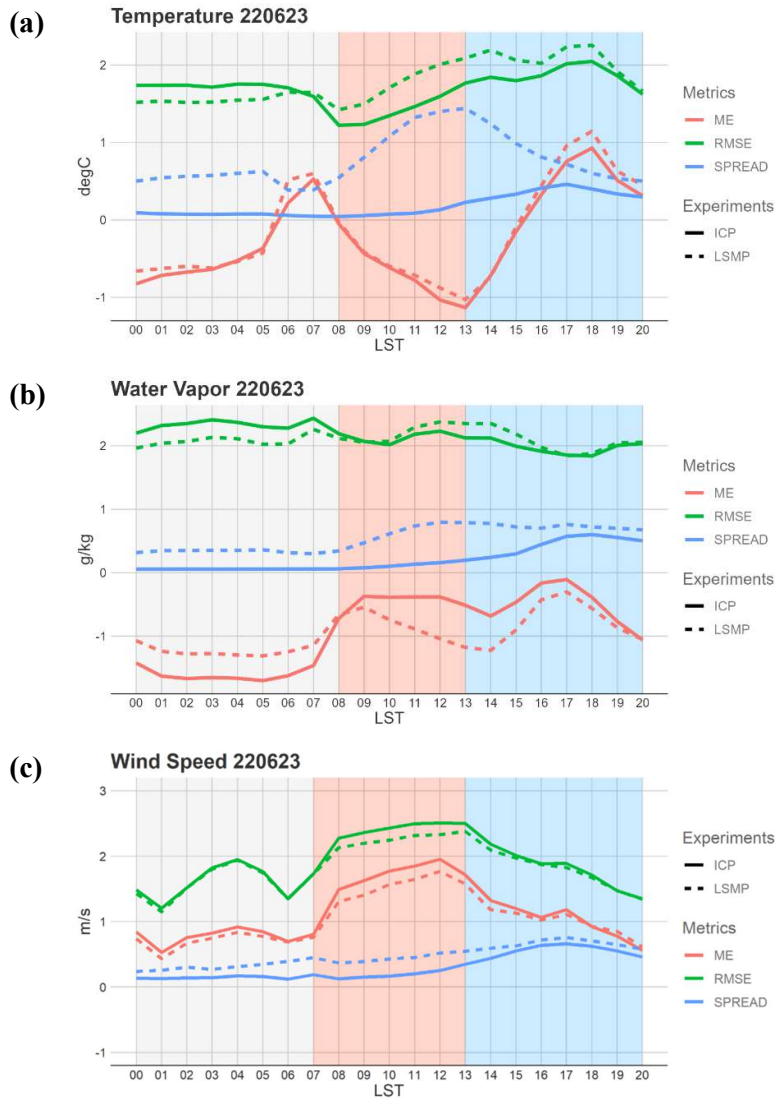
FIG. 4.11 Verification of (a) 2-m temperature , (b) 2-m water vapor at 2-meter height, and 10-m wind speed at10 meter height for the case 23, June 2022. Red, green, and blue lines represent the mean error, root mean square error, and spread of the ensemble model, respectively. Solid lines stand for the ICP experiment, and dashed lines represent the LSMP experiment.

41
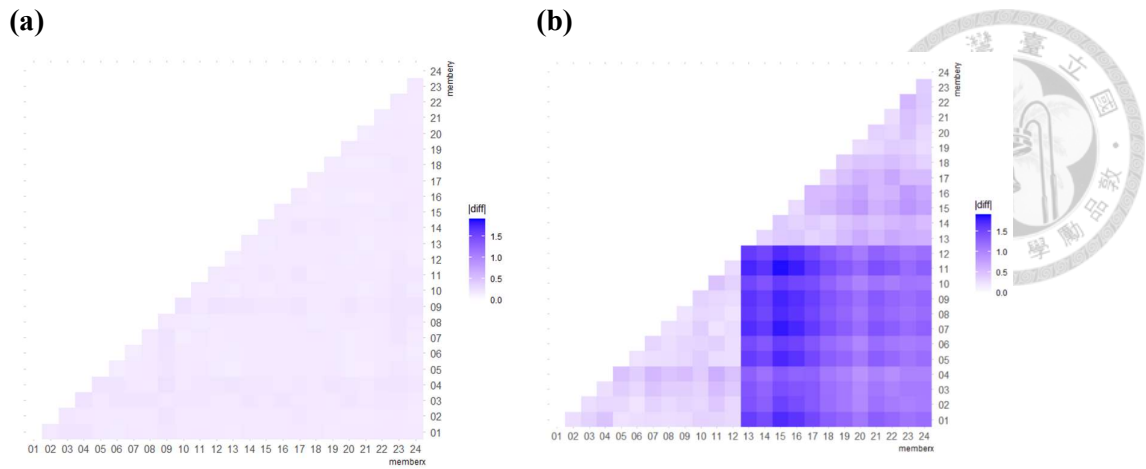
FIG. 4.12 The inter-member differences of water vapor at 2-m within the experiment of (a) ICP and (b) LSMP, the x-axis and y-axis numbers correspond to member serial number. 01~12 members apply M-O scheme of opt_sfc, and 13~24 member apply Noah scheme of opt_sfc.
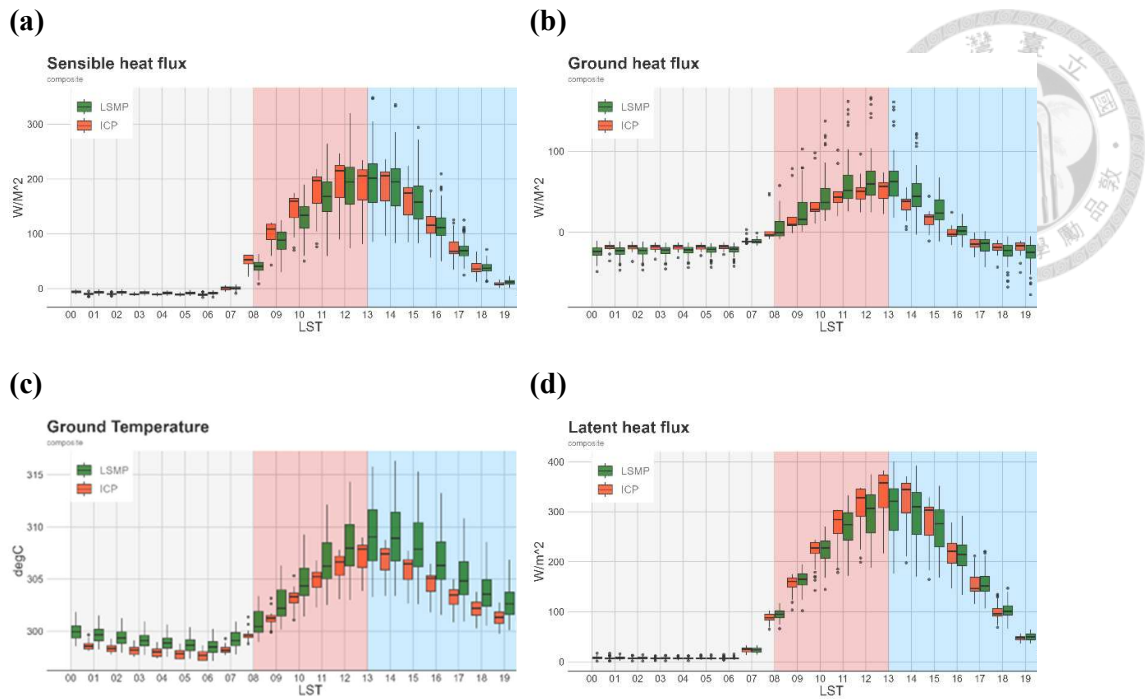
FIG. 4.13 The composite result of diurnal variation in (a) sensible heat flux exchange coefficient, (b) ground heat flux, (c) ground temperature, and (d) latent heat flux.
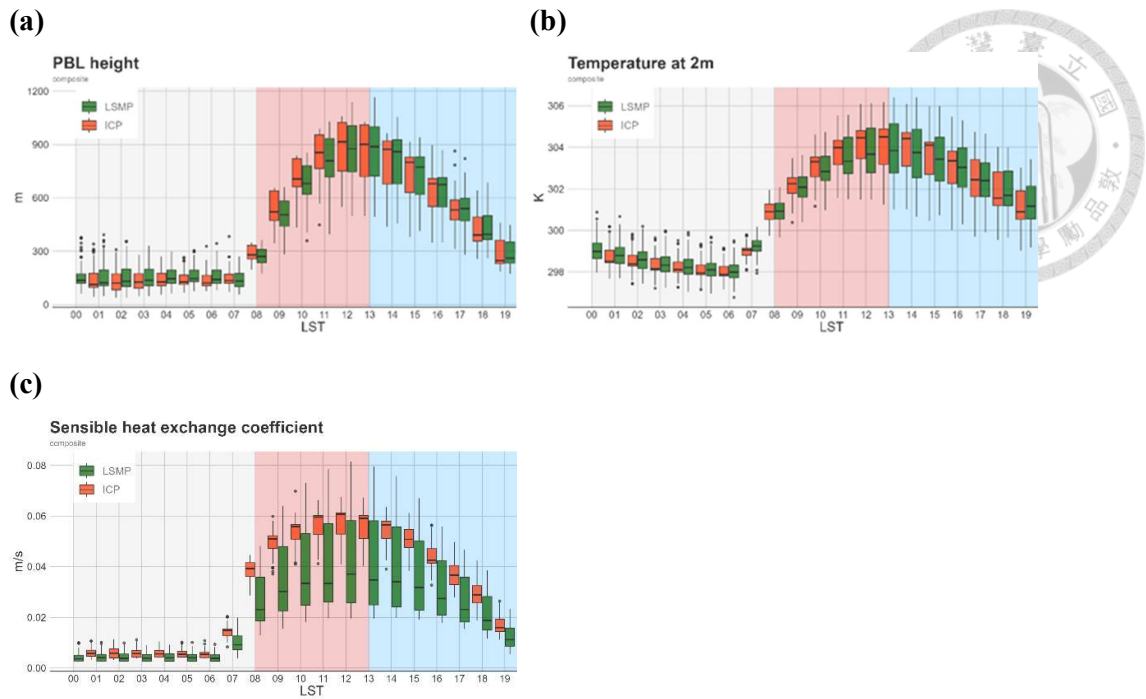
FIG. 4.14 The composite result of the diurnal variation in (a) planetary boundary layer height, (b) temperature at 2 meters height, and (c) sensible heat exchange coefficients.
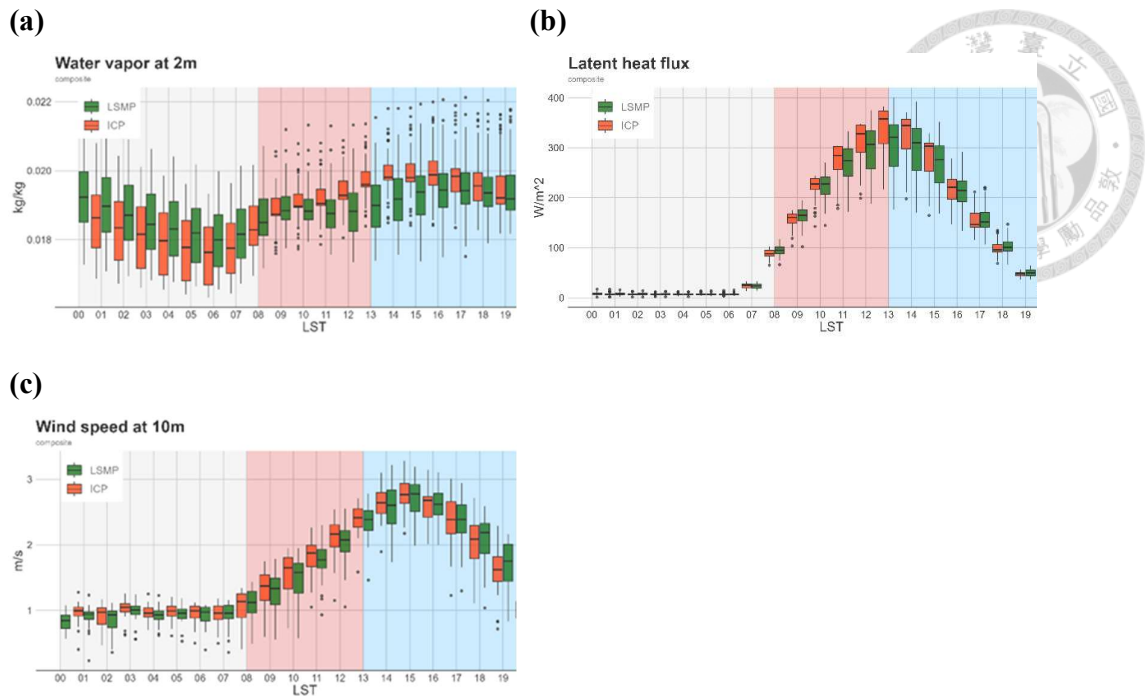
FIG. 4.15 The composite result of the diurnal variation in (a) water vapor at 2 meters height, (b) latent heat flux, and (c) wind speed at 10 meters height.

5. Discussion

5.1 Ensemble clustering

Previous studies have indicated that ensemble systems with multi-physics designs may exhibit characteristics of clustering among ensemble members (Li and Hong 2014). This study identified a similar classification patterns as discussed in Section 4.3. The analysis shown in Fig. 4.12, reveal that the most influential option to result in the clustering of the ensemble members in LSMP is opt_sfc, which governs the coefficient for sensible heat flux (C_H). Two schemes, namely the M-O scheme and the Noah scheme in opt_sfc, are utilized in the LSMP experiment.

C_H directly affects the calculation of sensible heat flux, and there are half of the members in LSMP implement the Noah scheme, which generally yields lower C_H values compared to the M-O scheme. Consequently, compared with ICP experiment, LSMP exhibites lower sensible heat flux and led to reduced planetary boundary layer height (PBLH) and lower 2-m temperature, and may change the local circulation further affecting water vapor in the boundary layer (Section 4.2).

The details of M-O scheme and Noah scheme are presented below

$$\text{Noah scheme: } C_H = \frac{\kappa^2}{\left[ln\left(\frac{Z}{Z_{0m}}\right)-\psi_m\left(\frac{Z}{L}\right)+\psi_m\left(\frac{Z_{0m}}{L}\right)\right]\left[ln\left(\frac{Z}{Z_{0h}}\right)-\psi_h\left(\frac{Z}{L}\right)+\psi_h\left(\frac{Z_{0h}}{L}\right)\right]} \qquad (5.1)$$

$$\text{M-O scheme: } C_H = \frac{\kappa^2}{\left[ln\left(\frac{z-d_0}{z_{0m}}\right)-\psi_m\left(\frac{z-d_0}{L}\right)\right]\left[ln\left(\frac{z-d_0}{z_{0h}}\right)-\psi_h\left(\frac{z-d_0}{L}\right)\right]} \qquad (5.2)$$

$$\text{In M-O scheme: } Z_{oh} = Z_{om} \qquad (5.3)$$

$$\text{In Noah scheme: } Z_{oh} = Z_{om} \, exp \, exp \left(-kC_{zil}\sqrt{R_e}\right), R_e = \frac{u_0^* Z_{om}}{v} \qquad (5.4)$$

In both schemes, where κ is the von Kármán constant, L is the Monin-Obukhov length, and z is the reference height. Z_{0h} and Z_{0m} are roughness lengths for heat and momentum, respectively, Re is the roughness Reynolds number, and d_0 is the zero-displacement height equal to 0.65 times canopy height.
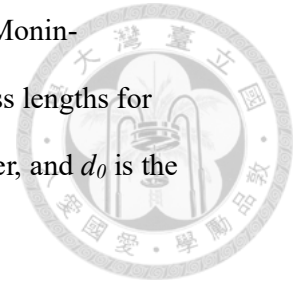
Except for including the d_0 (the impact is limited, not shown here), the major difference between M-O and Noah schemes is the design of the Z_{0h}. In the M-O scheme, Z_{0h} is identical to Z_{0m} (5.3), which means roughness lengths for heat borrow the concept of the roughness lengths for momentum. In the Noah scheme, Z_{0h} was applied by a modulation based on the Z_{0m} (Niu et al. 2011).

In the LSMP experiment, half of the members apply the M-O scheme, while the other half apply the Noah scheme. The diurnal cycle of the C_H for LSMP members is presented in Fig. 5.1. The results show that the M-O scheme exhibits significantly higher C_H values compared to the Noah scheme, with lower spread. The difference in C_H between the M-O and Noah schemes leads to a clustering pattern observed in Fig. 4.12. On the other hand, all members in the ICP experiment apply the M-O scheme. In the LSMP experiment, the members consist of both the M-O scheme and the Noah scheme, with the M-O scheme having a larger C_H and the Noah scheme having a smaller C_H. As a result, LSMP generally exhibits a more extensive spread and a smaller ensemble mean of C_H compared to ICP, as shown in Fig. 4.14.c.

5.2 Czil parameter

Notably, the Noah scheme incorporates an empirical parameter *Czil* in calculating Z_{0h} (5.4) which has a significant influence on the sensible heat flux, and therefore is sensitive to LSM processes in the Noah MP model (Duda et al., 2017;

Zhang et al., 2022). In this study, we conducted three experiments for the case on June 24, 2022, using LSMP configurations with $Czil$ values of 0.01, 0.03, and 0.1, as shown in Fig. 5.2.
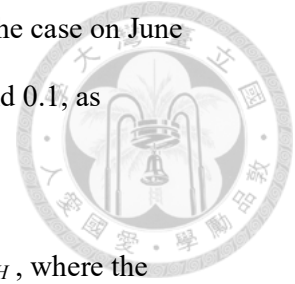
The results demonstrate that the $Czil$ has a notable impact on C_H, where the larger $Czil$ leads to lower C_H, indicating the weaker coupling between land and atmosphere due to the enhanced sensible heat transfer in certain land-air temperature gradients. This suggests that tuning the $Czil$ parameter may be crucial for improving model predictions. Moreover, the sensitivity of $Czil$ also highlights its potential as a perturbation scheme design in LSM. However, further research is needed to fully explore this potential.

5.3 Comparison with microphysics-based ensemble system

In addition to comparing the spread induced by LSM perturbation with atmospheric initial condition perturbation, this research aims to explore the effects of LSM perturbation in combination with other physics-based perturbations. To gain a more comprehensive understanding, we also make a rough comparison with the study conducted by Chen et al. (2022). They conducted ensemble experiments focusing on multi-physics microphysical perturbations to investigate the sensitivity of convective heavy rain simulation to cloud microphysical parameterization. Notably, their and this research both focused on afternoon thunderstorms in Taiwan using the WRF model, while the selected cases model configuration and ensemble size are all different.

Figure 5.3 provides a comparison of coefficient of variation of spatially averaged accumulated rainfall over ensemble system between LSMP in our research and in the microphysics-based ensemble conducted by Chen et al. (2022). The

48

coefficient of variation is calculated separately for five and ten cases and then averaged. The results demonstrate that the LSM induced mean precipitation standard deviation is approximately half that of the microphysics ensemble. This finding suggests that LSM perturbation may still plays a significant role in ensemble systems, even when compared to microphysics-based perturbations.
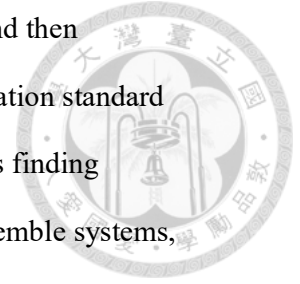
In comparing the spread induced by multi-physics LSMP and multi-physics microphysics, it is important to consider their respective impacts on ensemble predictions. The multi-physics LSMP perturbation scheme primarily affects land surface processes, such as surface heat fluxes and SM, influencing the atmospheric boundary layer and moisture availability. On the other hand, the multi-physics microphysics scheme focuses on the parameterization of cloud and precipitation processes, including cloud microphysics and the treatment of rain and ice particles.

49
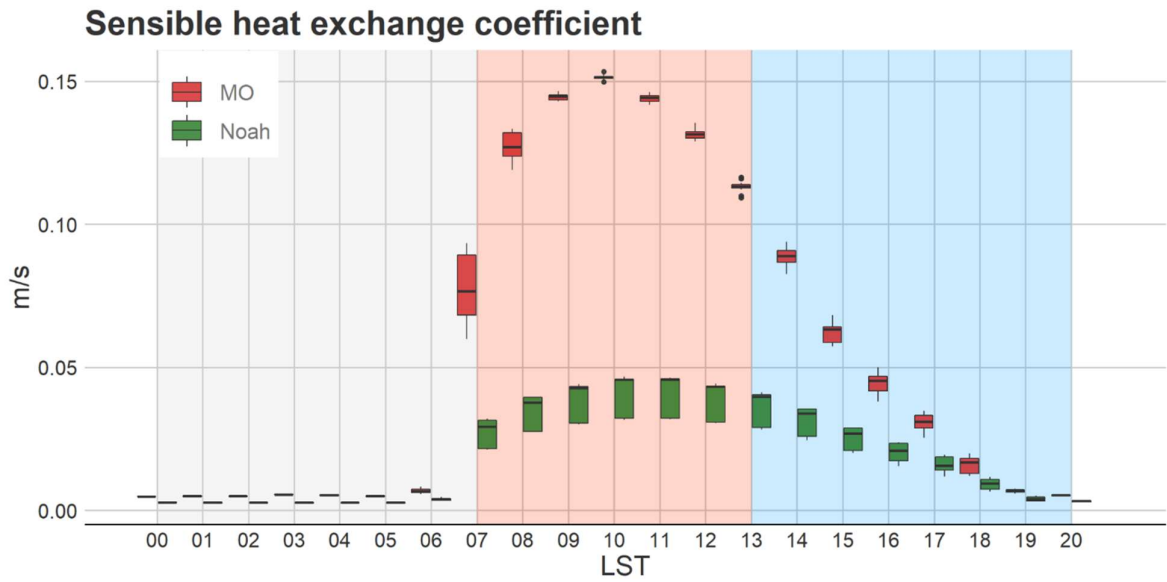
FIG. 5.1 The diurnal cycle of the spatial average of sensible heat exchange

coefficient. The red and green boxplot represent distributions of ensemble members in

LSMP applying M-O scheme and Noah scheme, respectively.

FIG. 5.2 The diurnal cycle of the spatial average of sensible heat exchange coefficient. The green, red, and yellow boxplot represent distributions of ensemble applying Czil of value 0.01, 0.03, and 0.1, respectively. Each ensemble consist of 12 members whose configuration is followed by LSMP members applying the Noah scheme.

Mean Coefficient of Variation for Accumulated Rainfall
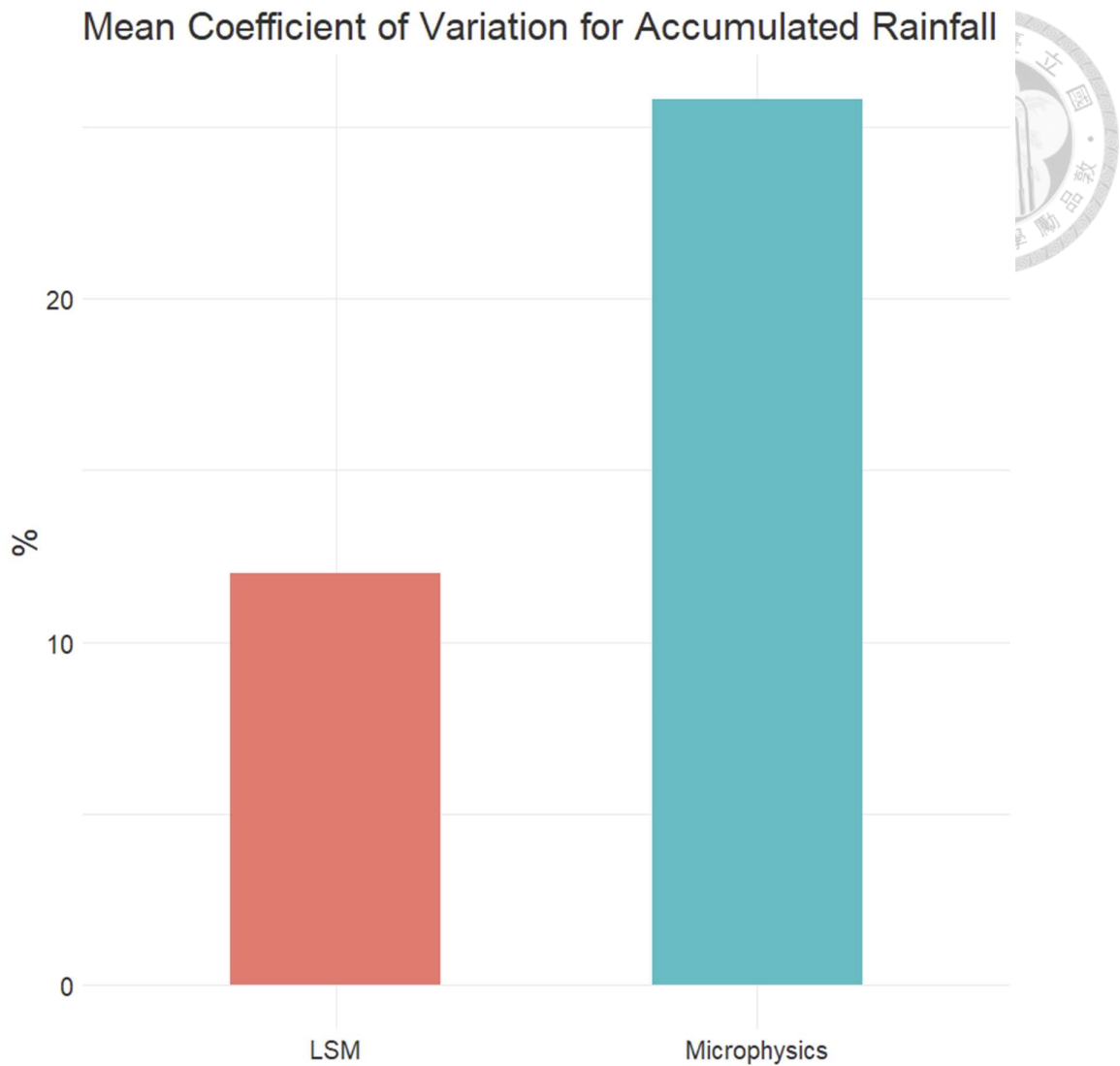
FIG 5.3 Comparison of coefficient of variation of spatially averaged accumulated rainfall over ensemble system between LSMP in our research and the micr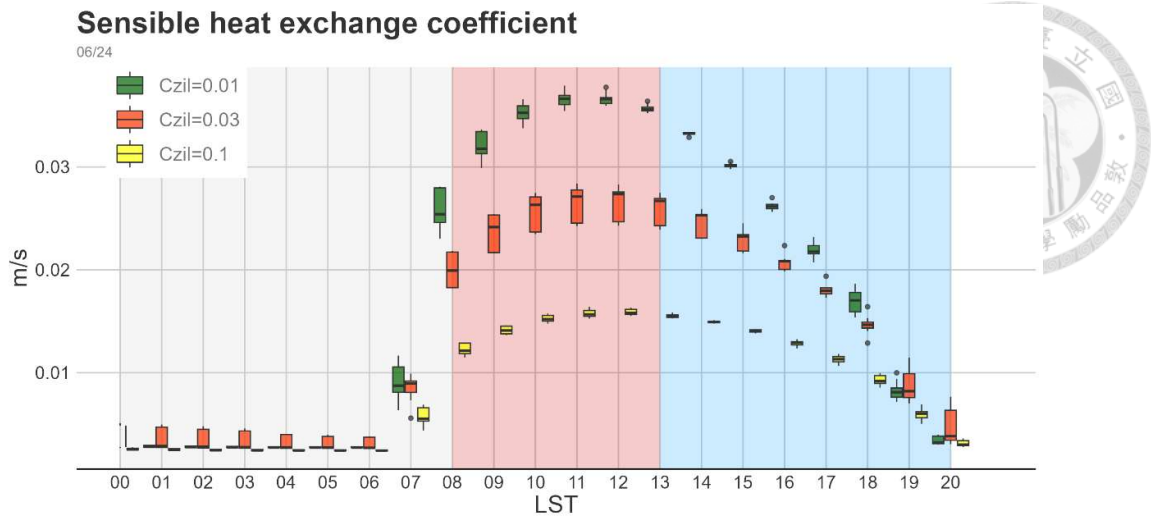ophysics-based ensemble conducted by Chen et al. (2022). The coefficient of variation is calculated separately for five and ten cases and then averaged.

52

6. Conclusion

In Taiwan's warm seasons, afternoon thunderstorms (ATs) can produce intense rainfall, which may result in the loss of property and human life, while it is also essential for water resources management. Therefore, how to predict the precise location, timing, and intensity of ATs is a demanding issue in Taiwan. Numerous factors, such as land-sea breeze, orography-induced flows, and anabatic flows, impact the structure and evolution of ATs in Taiwan. Moreover, the nonlinear nature of rapidly evolving convections imposes limitations on the predictability of models within a few hours. Solely relying on the output from a deterministic prediction can result in inadequate forecasts. However, ensemble prediction is expected to improve ATs predictability and offer information on forecast uncertainty.

Under weak synoptic conditions, the LAI is critical for the evolution and forecasting of ATs. The treatment of land and vegetation processes within LSMs determines surface sensible and latent heat fluxes, convective mixing, boundary layer growth, and the transport of moisture into the upper troposphere. Therefore, the LAI may be an important source of uncertainty in ensemble ATs predictions. In this study, we apply Noah MP and WRF model to investigate the impact of LSM perturbation on afternoon thunderstorm ensemble prediction.

First of all, this research conducts offline LSM experiments to understand better the physical processes that control the behavior of land surfaces and their interactions with the atmosphere and acquire a more realistic LSM state. We use high-resolution land surface characteristic data, including soil texture, land cover, vegetation fraction, and terrain height, to realistically illustrate the interface between land and atmosphere.

Offline experiments are driven by hourly atmospheric forcing data of 1 km resolution consisting of temperature, water vapor, wind speed, surface pressure, radiation, and precipitation. Specifically, temperature, water vapor, wind speed, longwave radiation, and surface pressure data are sourced from the CWB WRF 12-23 hour forecast. Short wave radiation data is sourced from remote sensing data from three channels, B03, B13, and B15, of the Himawari-8 geostationary satellite. Precipitation data are obtained from QPE. The QPE product is adopted from the
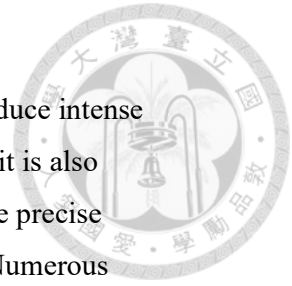
53

Quantitative Precipitation Estimation and Segregation Using Multiple Sensors (QPESUMS) system. The primary conclusion includes:
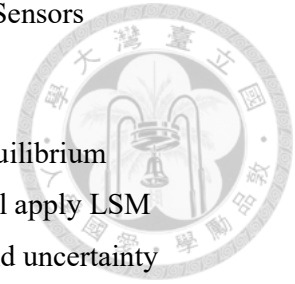
1. For the investigation of spin-up behavior, the LSM reaches equilibrium within three months. Therefore, the following experiments will apply LSM initial conditions after spin-up for at least three months to avoid uncertainty in LSM initial conditions.

2. The NOARAIN experiment generally gets a higher option spread than CTRL for the sensitivity experiment. Moreover, the sensitivity experiment results suggest that the top four options with the highest spread are opt_sfc, opt_rad, opt_crs, and opt_rsf, and we apply these four options to compose our LSM perturbation scheme.

Based on the offline result, we perform two 1-km resolution WRF afternoon thunderstorm ensemble experiments, where ICP considers initial condition perturbation only, and LSMP involves initial condition and LSM perturbation, and each experiment comprises 24 members. Five afternoon thunderstorm cases are simulated in this study. A detailed case study on June 24 2022 and composite results over five cases are presented in this study, as summarized below:

1. The LSMP experiment demonstrates a broader range of variability in precipitation, suggesting that the LSM perturbation plays a role in the spread of ensemble precipitation prediction. However, ICP and LSMP underpredict the precipitation amount and provide premature predictions of rainfall initiation and peak timing. The median of the two experiments is comparable, indicating that LSM perturbation weakly affects the mean precipitation of the ensemble system in our study. It is suggested that additional investigations, such as improvement of initial/boundary conditions and atmospheric physics processes, may be necessary to improve the precipitation forecast (Tong et al., 2016).

2. Regarding the ensemble mean, the diagnostic analysis reveals that ICP exhibits higher sensible heat flux in the pre-storm phase, resulting in elevated temperatures in the lower atmosphere; Consequently, stronger in-land winds are induced, accompanied by higher 2-m water vapor in the lower altitude

54

region. The verification analysis demonstrates that the root mean square error (RMSE) for LSMP shows a slight increase, potentially attributed to higher mean error values.

3. In terms of spread, LSMP demonstrates a wider range compared to ICP across various variables. The primary source of this variability in LSMP is attributed to opt_sfc, which encompasses both M-O and Noah schemes and determines the exchange coefficient for sensible heat. Besides, opt_sfc leads to classifying ensemble members in LSMP by the M-O scheme and Noah scheme.

4. Notably, one of the important differences between the Noah scheme and the M-O scheme is roughness length formulation which the Noah scheme cooperating CZIL parameter in its algorithm; therefore, we evaluate the sensitivity of the CZIL parameter on sensible heat flux in the Noah scheme and demonstrate that CZIL can be an important source of uncertainty in LSMs, revealing its potential in LSM-based perturbation scheme design.

In summary, this research first focuses on evaluating the sensitivity of physical processes to ensemble spread and spin-up behavior of the Noah MP through offline experiments. Building upon the offline results, we obtain a more realistic representation of the land surface state and configure an LSM-based perturbation scheme. We proceed to perform ensemble predictions of afternoon thunderstorms at a 1-kilometer resolution and assess the impact of the perturbation scheme based on the LSM. Based on the present works, we proposed several issues for future research:

1. Expand the number of cases: The current five cases may not provide sufficient coverage and representativeness. Therefore, it is essential to include more cases in future studies to enhance the robustness and reliability of the findings. By incorporating a broader range of scenarios, we can better understand the model's performance and ability to capture different meteorological conditions.

2. Addressing the influence of CZIL: The CZIL parameter has been identified as a significant factor influencing the model results (Chen et al., 1997). Exploring approaches for properly handling CZIL is crucial to improve the model's accuracy. Additionally, given its impact on the model results, CZIL also holds the potential for further development as a perturbation scheme.

3. Optimal integration of LSM and other physics schemes: Exploring the strategies to effectively integrate LSM with other physics schemes, such as surface layer, boundary layer turbulence, and microphysics scheme, is an essential avenue for future research.

4. Enhanced probabilistic verification: In addition to traditional deterministic verification methods, there is a need to expand the analysis to include more probabilistic verification techniques. These methods consider the uncertainty inherent in the model outputs and provide a more comprehensive assessment of the model's predictive skill. By incorporating probabilistic verification, we can better understand the model's reliability in capturing the variability and likelihood of different weather events.
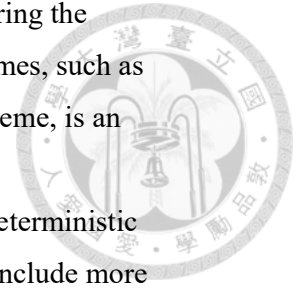
Reference

Ajami, H., M. McCabe, J. Evans, and S. Stisen, 2014: Assessing the impact of model spin-up on surface water-groundwater interactions using an integrated hydrologic model. *Water Resources Research*, **50**, 2636–2656, https://doi.org/10.1002/2013WR014258.

Anthes, R. A., 1984: Enhancement of Convective Precipitation by Mesoscale Variations in Vegetative Covering in Semiarid Regions. *Journal of Applied Meteorology and Climatology*, **23**, 541–554, https://doi.org/10.1175/1520-0450(1984)023<0541:EOCPBM>2.0.CO;2.

Barker, D. M., 2005: Southern High-Latitude Ensemble Data Assimilation in the Antarctic Mesoscale Prediction System. *Monthly Weather Review*, **133**, 3431–3449, https://doi.org/10.1175/MWR3042.1.

Basara, J. B., 2001: The value of point-scale measurements of soil moisture in planetary boundary layer simulations. Ph.D. dissertation, University of Oklahoma, 225 pp.

Bhattacharya, A., A. N. V. Satyanarayana, and M. M, 2018: Impact of Land Surface and Forcing Parameters on the Spin-up Behaviour of Noah Land Surface Model over the Indian Sub-Continent. *Pure Appl. Geophys.*, **175**, 389–401, https://doi.org/10.1007/s00024-017-1645-4.

Chang, H.-L., B. G. Brown, P.-S. Chu, Y.-C. Liou, and W.-H. Wang, 2017: Nowcast Guidance of Afternoon Convection Initiation for Taiwan. *Weather and Forecasting*, **32**, 1801–1817, https://doi.org/10.1175/WAF-D-16-0224.1.

Chang, M., W. Liao, X. Wang, Q. Zhang, W. Chen, Z. Wu, and Z. Hu, 2020: An optimal ensemble of the Noah-MP land surface model for simulating surface heat fluxes over a typical subtropical forest in South China. *Agricultural and Forest Meteorology*, **281**, 107815, https://doi.org/10.1016/j.agrformet.2019.107815.

Chang, P.-L., and Coauthors, 2021: An Operational Multi-Radar Multi-Sensor QPE System in Taiwan. *Bulletin of the American Meteorological Society*, **102**, E555–E577, https://doi.org/10.1175/BAMS-D-20-0043.1.

Chen, C.-S., Y.-L. Chen, C.-L. Liu, P.-L. Lin, and W.-C. Chen, 2007: Statistics of Heavy Rainfall Occurrences in Taiwan. *Weather and Forecasting*, **22**, 981–1002, https://doi.org/10.1175/WAF1033.1.

Chen, F., and J. Dudhia, 2001: Coupling an Advanced Land Surface–Hydrology Model with the Penn State–NCAR MM5 Modeling System. Part I: Model Implementation and Sensitivity. *Monthly Weather Review*, **129**, 569–585, https://doi.org/10.1175/1520-0493(2001)129<0569:CAALSH>2.0.CO;2.

——, Z. Janjić, and K. Mitchell, 1997: Impact of Atmospheric Surface-layer Parameterizations in the new Land-surface Scheme of the NCEP Mesoscale Eta Model. *Boundary-Layer Meteorology*, **85**, 391–421, https://doi.org/10.1023/A:1000531001463.

Chen, J.-P., T.-C. Tsai, M.-D. Tzeng, C.-S. Liao, H.-C. Kuo, and J.-S. Hong, 2022: Microphysical Perturbation Experiments and Ensemble Forecasts on Summertime Heavy Rainfall over Northern Taiwan. Weather and Forecasting, 37, 1641–1659, https://doi.org/10.1175/WAF-D-22-0004.1.

Chen, T.-C., M.-C. Yen, J.-D. Tsay, C.-C. Liao, and E. S. Takle, 2014: Impact of Afternoon Thunderstorms on the Land–Sea Breeze in the Taipei Basin during Summer: An Experiment. *Journal of Applied Meteorology and Climatology*, **53**, 1714–1738, https://doi.org/10.1175/JAMC-D-13-098.1.

——, J.-D. Tsay, and E. S. Takle, 2016: A Forecast Advisory for Afternoon Thunderstorm Occurrence in the Taipei Basin during Summer Developed from Diagnostic Analysis. *Weather and Forecasting*, **31**, 531–552, https://doi.org/10.1175/WAF-D-15-0082.1.

Chen, Y., K. Yang, D. Zhou, J. Qin, and X. Guo, 2010: Improving the Noah Land Surface Model in Arid Regions with an Appropriate Parameterization of the Thermal Roughness Length. *Journal of Hydrometeorology*, **11**, 995–1006, https://doi.org/10.1175/2010JHM1185.1.

Chen, Y.-L., and J. Li, 1995: Characteristics of Surface Airflow and Pressure Patterns over the Island of Taiwan during TAMEX. *Monthly Weather Review*, **123**, 695–716,
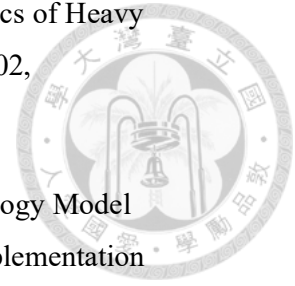
https://doi.org/10.1175/1520-0493(1995)123<0695:COSAAP>2.0.CO;2.

Cheng, K.-H., T.-Y. Yeh, M.-C. Weng, L.-N. Shee, H.-C. Chang, and Y.-C. Chang, 2021: Surface Solar Irradiance Estimation in Taiwan by Using Himawari-8 Satellite. *2021 Conference on Weather Analysis and Forecasting*. (In Chinese, accessed at https://reurl.cc/940peX)

Cosgrove, B. A., and Coauthors, 2003: Land surface model spin-up behavior in the North American Land Data Assimilation System (NLDAS). *Journal of Geophysical Research: Atmospheres*, **108**, https://doi.org/10.1029/2002JD003316.

Dirmeyer, P., X. Gao, M. Zhao, Z. Guo, T. Oki, and N. Hanasaki, 2006a: GSWP-2: Multimodel Analysis and Implications for Our Perception of the Land Surface. *Bulletin of The American Meteorological Society - BULL AMER METEOROL SOC*, **87**, 1381–1398, https://doi.org/10.1175/BAMS-87-10-1381.

——, R. Koster, and Z. Guo, 2006b: Do Global Models Properly Represent the Feedback between Land and Atmosphere? *Journal of Hydrometeorology - J HYDROMETEOROL*, **7**, 1177–1198, https://doi.org/10.1175/JHM532.1.

Duda, J. D., X. Wang, and M. Xue, 2017: Sensitivity of Convection-Allowing Forecasts to Land Surface Model Perturbations and Implications for Ensemble Design. *Monthly Weather Review*, **145**, 2001–2025, https://doi.org/10.1175/MWR-D-16-0349.1.

Ek, M. B., K. E. Mitchell, Y. Lin, E. Rogers, P. Grunmann, V. Koren, G. Gayno, and J. D. Tarpley, 2003: Implementation of Noah land surface model advances in the National Centers for Environmental Prediction operational mesoscale Eta model. *Journal of Geophysical Research: Atmospheres*, **108**, https://doi.org/10.1029/2002JD003296.

Entin, J. K., A. Robock, K. Y. Vinnikov, V. Zabelin, S. Liu, A. Namkhai, and Ts. Adyasuren, 1999: Evaluation of Global Soil Wetness Project Soil Moisture Simulations. *Journal of the Meteorological Society of Japan*, **77**, 183–198, https://doi.org/10.2151/jmsj1965.77.1B_183.

Godfrey, C. M., and D. J. Stensrud, 2010: An Empirical Latent Heat Flux Parameterization for the Noah Land Surface Model. *Journal of Applied Meteorology and Climatology*,

49, 1696–1713, https://doi.org/10.1175/2010JAMC2180.1.
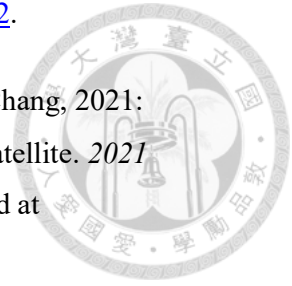
Guo, Z., P. A. Dirmeyer, Z.-Z. Hu, X. Gao, and M. Zhao, 2006: Evaluation of the Second Global Soil Wetness Project soil moisture simulations: 2. Sensitivity to external meteorological forcing. *Journal of Geophysical Research: Atmospheres*, **111**, https://doi.org/10.1029/2006JD007845.

Hermoso, A., V. Homar Santaner, and R. Plant, 2021: Potential of stochastic methods for improving convection-permitting ensemble forecasts of extreme events over the Western Mediterranean. *Atmospheric research*, **257**, 105571, https://doi.org/10.1016/j.atmosres.2021.105571.

Hirt, M., and G. C. Craig, 2021: A cold pool perturbation scheme to improve convective initiation in convection-permitting models. *Quarterly Journal of the Royal Meteorological Society*, **147**, 2429–2447, https://doi.org/10.1002/qj.4032.

——, S. Rasp, U. Blahak, and G. C. Craig, 2019: Stochastic Parameterization of Processes Leading to Convective Initiation in Kilometer-Scale Models. *Monthly Weather Review*, **147**, 3917–3934, https://doi.org/10.1175/MWR-D-19-0060.1.

——, G. C. Craig, S. A. K. Schäfer, J. Savre, and R. Heinze, 2020: Cold-pool-driven convective initiation: using causal graph analysis to determine what convection-permitting models are missing. *Quarterly Journal of the Royal Meteorological Society*, **146**, 2205–2227, https://doi.org/10.1002/qj.3788.

Hong, S.-Y., Y. Noh, and J. Dudhia, 2006: A New Vertical Diffusion Package with an Explicit Treatment of Entrainment Processes. *Monthly Weather Review*, **134**, 2318–2341, https://doi.org/10.1175/MWR3199.1.

Hung, Y.-C., J.-S. Hong, C.-L. Tsay, M. Barlage, and F. Chen, 2014: Evaluation of the High Resolution Land Data Assimilation System. *Atmospheric Sciences*, **42**, 29–48. (In Chinese)

Iacono, M. J., J. S. Delamere, E. J. Mlawer, M. W. Shephard, S. A. Clough, and W. D. Collins, 2008: Radiative forcing by long-lived greenhouse gases: Calculations with the AER radiative transfer models. *Journal of Geophysical Research: Atmospheres*,

113, https://doi.org/10.1029/2008JD009944.

Jackson, C., Y. Xia, M. K. Sen, and P. L. Stoffa, 2003: Optimal parameter and uncertainty
estimation of a land surface model: A case study using data from Cabauw,
Netherlands. *Journal of Geophysical Research: Atmospheres*, **108**,
https://doi.org/10.1029/2002JD002991.
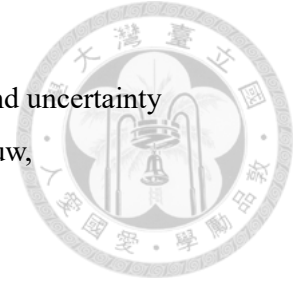
Johnson, R. H., and J. F. Bresch, 1991: Diagnosed Characteristics of Precipitation Systems
over Taiwan during the May–June 1987 TAMEX. *Monthly Weather Review*, **119**,
2540–2557, https://doi.org/10.1175/1520-0493(1991)119<2540:DCOPSO>2.0.CO;2.

Jou, B., 1994: Mountain-Originated Mesoscale Precipitation System in Northern Taiwan: A
Case Study 21 June 1991. *Terrestrial Atmospheric and Oceanic Sciences*, **5**, 169–197,
https://doi.org/10.3319/TAO.1994.5.2.169(TAMEX).

Koster, R. D., Z. Guo, R. Yang, P. A. Dirmeyer, K. Mitchell, and M. J. Puma, 2009: On the
Nature of Soil Moisture in Land Surface Models. *Journal of Climate*, **22**, 4322–4335,
https://doi.org/10.1175/2009JCLI2832.1.

Kumar, A., F. Chen, D. Niyogi, J. G. Alfieri, M. Ek, and K. Mitchell, 2011: Evaluation of a
Photosynthesis-Based Canopy Resistance Formulation in the Noah Land-Surface
Model. *Boundary-Layer Meteorol*, **138**, 263–284, https://doi.org/10.1007/s10546-010-
9559-z.

LeMone, M. A., M. Tewari, F. Chen, J. G. Alfieri, and D. Niyogi, 2008: Evaluation of the
Noah Land Surface Model Using Data from a Fair-Weather IHOP_2002 Day with
Heterogeneous Surface Fluxes. *Monthly Weather Review*, **136**, 4915–4941,
https://doi.org/10.1175/2008MWR2354.1.

Li, C.-H., and J.-S. Hong, 2014: The Study of Regional Ensemble Forecast: Evaluation for
the performance of perturbed methods. *Atmospheric Sciences*, **42**, 153–179. (In
Chinese)

Li, J., F. Chen, X. Lu, W. Gong, G. Zhang, and Y. Gan, 2020: Quantifying Contributions of
Uncertainties in Physical Parameterization Schemes and Model Parameters to Overall
Errors in Noah-MP Dynamic Vegetation Modeling. *Journal of Advances in Modeling*

Earth Systems, **12**, e2019MS001914, https://doi.org/10.1029/2019MS001914.

Lin, P.-F., P.-L. Chang, B. J.-D. Jou, J. W. Wilson, and R. D. Roberts, 2011: Warm Season Afternoon Thunderstorm Characteristics under Weak Synoptic-Scale Forcing over Taiwan Island. *Weather and Forecasting*, **26**, 44–60, https://doi.org/10.1175/2010WAF2222386.1.

Lin, T.-S., and F.-Y. Cheng, 2016: Impact of Soil Moisture Initialization and Soil Texture on Simulated Land–Atmosphere Interaction in Taiwan. *Journal of Hydrometeorology*, **17**, 1337–1355, https://doi.org/10.1175/JHM-D-15-0024.1.

Marshall, C. H., K. C. Crawford, K. E. Mitchell, and D. J. Stensrud, 2003: The Impact of the Land Surface Physics in the Operational NCEP Eta Model on Simulating the Diurnal Cycle: Evaluation and Testing Using Oklahoma Mesonet Data. *Weather and Forecasting*, **18**, 748–768, https://doi.org/10.1175/1520-0434(2003)018<0748:TIOTLS>2.0.CO;2.

Melhauser, C., and F. Zhang, 2012: Practical and Intrinsic Predictability of Severe and Convective Weather at the Mesoscales. *Journal of the Atmospheric Sciences*, **69**, 3350–3371, https://doi.org/10.1175/JAS-D-11-0315.1.

Niu, G.-Y., and Coauthors, 2011: The community Noah land surface model with multiparameterization options (Noah-MP): 1. Model description and evaluation with local-scale measurements. *Journal of Geophysical Research: Atmospheres*, **116**, https://doi.org/10.1029/2010JD015139.

Peters, K., C. Hohenegger, and D. Klocke, 2019: Different Representation of Mesoscale Convective Systems in Convection-Permitting and Convection-Parameterizing NWP Models and Its Implications for Large-Scale Forecast Evolution. *Atmosphere*, **10**, 503, https://doi.org/10.3390/atmos10090503.

Pielke Sr., R. A., 2001: Influence of the spatial distribution of vegetation and soils on the prediction of cumulus Convective rainfall. *Reviews of Geophysics*, **39**, 151–177, https://doi.org/10.1029/1999RG000072.

Pitman, A. J., 2003: The evolution of, and revolution in, land surface schemes designed for

climate models. *International Journal of Climatology*, **23**, 479–510, https://doi.org/10.1002/joc.893.

Rodell, M., P. R. Houser, A. A. Berg, and J. S. Famiglietti, 2005: Evaluation of 10 Methods for Initializing a Land Surface Model. *J. Hydrometeorol.*, **6**, 146–155, https://doi.org/10.1175/jhm414.1.

Rotunno, R., J. B. Klemp, and M. L. Weisman, 1988: A Theory for Strong, Long-Lived Squall Lines. *Journal of the Atmospheric Sciences*, **45**, 463–485, https://doi.org/10.1175/1520-0469(1988)045<0463:ATFSLL>2.0.CO;2.

Seck, A., C. Welty, and R. Maxwell, 2015: Spin-up behavior and effects of initial conditions for an integrated hydrologic model: Spin-up behavior and effects of initial conditions. *Water Resources Research*, **51**, 2188–2210, https://doi.org/10.1002/2014WR016371.

Sellers, P. J., and Coauthors, 1996: A Revised Land Surface Parameterization (SiB2) for Atmospheric GCMS. Part I: Model Formulation. *Journal of Climate*, **9**, 676–705, https://doi.org/10.1175/1520-0442(1996)009<0676:ARLSPF>2.0.CO;2.

Shukla, J., and Y. Mintz, 1982: Influence of Land-Surface Evapotranspiration on the Earth's Climate. *Science*, **215**, 1498–1501, https://doi.org/10.1126/science.215.4539.1498.

Shuttleworth, W., E. Burke, P. Houser, D. Toll, M. Rodell, and K. Arsenault, 2006: Toward a South America Land Data Assimilation System: Aspects of land surface model spin-up using the Simplified Simple Biosphere. *Journal of Geophysical Research*, **111**, https://doi.org/10.1029/2005JD006297.

Sokol, Z., and P. Zacharov, 2012: Nowcasting of precipitation by an NWP model using assimilation of extrapolated radar reflectivity. *Quarterly Journal of the Royal Meteorological Society*, **138**, 1072–1082, https://doi.org/10.1002/qj.970.

Sun, J., S. B. Trier, Q. Xiao, M. L. Weisman, H. Wang, Z. Ying, M. Xu, and Y. Zhang, 2012: Sensitivity of 0–12-h Warm-Season Precipitation Forecasts over the Central United States to Model Initialization. *Weather and Forecasting*, **27**, 832–855,

https://doi.org/10.1175/WAF-D-11-00075.1.

Tao, W.-K., D. Wu, S. Lang, J. Chern, C. Peters-Lidard, A. Fridlind, and T. Matsui, 2016: High-resolution NU-WRF simulations of a deep convective-precipitation system during MC3E: Further Improvements and Comparisons between Goddard microphysics schemes and observations. *Journal of Geophysical Research: Atmospheres*, **121**, https://doi.org/10.1002/2015JD023986.

Tewari, M., and Coauthors, 2016: Implementation and verification of the united NOAH land surface model in the WRF model. *20th Conference on Weather Analysis and Forecasting/16th Conference on Numerical Weather Prediction*, 11–15.

Thompson, G., J. Berner, M. Frediani, J. A. Otkin, and S. M. Griffin, 2021: A Stochastic Parameter Perturbation Method to Represent Uncertainty in a Microphysics Scheme. *Monthly Weather Review*, **149**, 1481–1497, https://doi.org/10.1175/MWR-D-20-0077.1.

Tong, W., G. Li, J. Sun, X. Tang, and Y. Zhang, 2016: Design Strategies of an Hourly Update 3DVAR Data Assimilation System for Improved Convective Forecasting. *Weather and Forecasting*, **31**, 1673–1695, https://doi.org/10.1175/WAF-D-16-0041.1.

Trier, S. B., F. Chen, and K. W. Manning, 2004a: A Study of Convection Initiation in a Mesoscale Model Using High-Resolution Land Surface Initial Conditions. *Monthly Weather Review*, **132**, 2954–2976, https://doi.org/10.1175/MWR2839.1.

——, ——, and ——, 2004b: A Study of Convection Initiation in a Mesoscale Model Using High-Resolution Land Surface Initial Conditions. *Monthly Weather Review*, **132**, 2954–2976, https://doi.org/10.1175/MWR2839.1.

Trier, S. B., F. Chen, K. W. Manning, M. A. LeMone, and C. A. Davis, 2008: Sensitivity of the PBL and Precipitation in 12-Day Simulations of Warm-Season Convection Using Different Land Surface Models and Soil Wetness Conditions. *Monthly Weather Review*, **136**, 2321–2343, https://doi.org/10.1175/2007MWR2289.1.

——, M. A. LeMone, F. Chen, and K. W. Manning, 2011: Effects of Surface Heat and Moisture Exchange on ARW-WRF Warm-Season Precipitation Forecasts over the

Central United States. *Weather and Forecasting*, **26**, 3–25, https://doi.org/10.1175/2010WAF2222426.1.

Weckwerth, T. M., 2000: The Effect of Small-Scale Moisture Variability on Thunderstorm Initiation. *Monthly Weather Review*, **128**, 4017–4030, https://doi.org/10.1175/1520-0493(2000)129<4017:TEOSSM>2.0.CO;2.

Yang, Z.-L., and Coauthors, 2011: The community Noah land surface model with multiparameterization options (Noah-MP): 2. Evaluation over global river basins. *Journal of Geophysical Research: Atmospheres*, **116**, https://doi.org/10.1029/2010JD015140.

Zhang, F., C. Snyder, and R. Rotunno, 2002: Mesoscale Predictability of the "Surprise" Snowstorm of 24–25 January 2000. *Monthly Weather Review*, **130**, 1617–1632, https://doi.org/10.1175/1520-0493(2002)130<1617:MPOTSS>2.0.CO;2.

Zhang, F., A. M. Odins, and J. W. Nielsen-Gammon, 2006: Mesoscale Predictability of an Extreme Warm-Season Precipitation Event. *Weather and Forecasting*, **21**, 149–166, https://doi.org/10.1175/WAF909.1.

Zhang, X., L. Chen, Z. Ma, J. Duan, D. Dai, and H. Zhang, 2022: Effects of the surface coupling strength in the WRF/Noah-MP model on regional climate simulations over China. *Climate Dynamics*, **59**, 331–355, https://doi.org/10.1007/s00382-021-06129-5.